ABSTRACT

Title of dissertation: TEMPORAL DYNAMICS OF HOT-ELECTRONS IN METAL FILMS AND ALLOYS

Sarvenaz Memarzadeh
Doctor of Philosophy, 2021

Dissertation directed by: Professor Jeremy N. Munday
Department of Electrical Engineering

When light is coupled into a surface plasmon mode, it can either decay radiatively by emitting a photon or non-radiatively by transferring its energy to charge carriers with excessive kinetic energy, also known as the "hot-carriers." The photogenerated hot-carriers are promising for applications ranging from optoelectronic devices to renewable energy. For example, recently, hot-carrier-based solar cells have emerged as a next generation solar energy converter, which utilizes the photoexcited hot-carriers and offers simplicity of design and higher power conversion efficiency when compared to first-generation photovoltaic cells such as the silicon. Over the past decades, there have been significant efforts to increase the efficiency of hot-carrier-based devices by introducing novel approaches for generating these energetic carriers. It has been found that the hot-carrier relaxation time also plays a crucial role in determining the efficiency of these devices. Further, the fast thermalization process of hot-carriers is the primary loss mechanism in hot-carrier devices. Thus,

to maximize the device efficiency, we need to prolong the hot-carrier relaxation time before any thermalization process takes place, which leads to heat generation and hence efficiency loss of such devices. For other devices, e.g. ultrafast photodetectors, a short lifetime may be beneficial. Thus, the ability to control the hot-carrier lifetime is important.

In this dissertation, we first focus on measuring the hot-carrier lifetime in metal films and then offer new approaches for controlling the relaxation time of the excited hot-carriers. For the measurement, we develop our degenerate pump-probe spectroscopy setup using a Ti:Sapphire pulsed laser, enabling us to measure the ultrafast temporal response of the generated hot-carriers in the optical frequency range. Next, we look at the effect of the propagating surface plasmons on the relaxation dynamics of the excited carriers in a thin gold film. Furthermore, to analyze the temporal dynamics and extract the relaxation time from the pump-probe measurements, we combine the internal electric field profile resulting from surface plasmon coupling with the conventional two-temperature model. Our results show that coupling to the propagating surface plasmon enhances the hot-carrier relaxation time due to the electric field confinement within a gold film. Finally, we explore the relaxation time of the excited hot-carriers in AuAg and AuCu alloys with different material compositions. For this purpose, we fabricated thin films with different Au, Ag, and Cu compositions through the sputtering deposition process. We found that different alloy compositions affect the relaxation time, and in the case of the AuAg alloyed thin films, it can vary up to 8 times under constant pump fluency. These results provide new approaches for controlling the hot-carrier relaxation time

depending on the applications.

TEMPORAL DYNAMICS OF HOT-ELECTRONS IN METAL FILMS AND ALLOYS

by

Sarvenaz Memarzadeh

Dissertation submitted to the Faculty of the Graduate School of the
University of Maryland, College Park in partial fulfillment
of the requirements for the degree of
Doctor of Philosophy
2021

Advisory Committee:
Professor Jeremy N. Munday, Chair/Advisor
Professor Thomas E. Murphy
Professor Mohammad Hafezi
Professor Cheng Gong
Professor John Cumings

Dedication

Dedicated to my beloved parents, Sima and Mehdi.

Acknowledgments

There are numerous thanks to be given upon the completion of this dissertation. First, I would like to give my sincere thanks to my advisor, Prof. Jeremy Munday, for his support and insightful guidance throughout this dissertation. Without his countless support and patience, this dissertation could not be completed. I would also like to give a very special thanks to Prof. Thomas Murphy for giving me the opportunity to acquire many skills in his laboratory. Prof. Murphy's relentless support goes beyond, and I am deeply grateful for having the opportunity to perform the ultrafast measurements in his laboratory. I also would like to appreciate my other committee members, Prof. Hafezi, Prof. Gong, and Prof. Cumings for their valuable time and suggestions. I owe a special thanks to Dr. Yigit Aytac for his valuable advice and help to build the setup, and Dr. Jongbum Kim for his insightful discussions and comments on the modeling section. I would also like to express my appreciation to everyone in the ECE graduate and business office, especially Melanie Prange, Emily Irwin, and Vivian Lu, who made sure I have my financial support and insurance during my Ph.D. Of course, all my great friends and colleagues in MundayLab and Photonic Research Laboratory my thanks go out continually for your support. On a personal note, I would like to sincerely thank my parents, Mehdi and Sima, and my dearest brother Alireza and sister-in-law Tanaz for all their love. Finally, I would like to thank everyone in the Maryland Nanocenter - FabLab, Mark Lecates, Jonathan Hummel, John Abrahams, and Tom Loughran for their training and helps. This work was supported by the National Science

Foundation under Grant No. (CAREER ECCS-1554503, MMN-2016617, MMN-1609414), Office of Naval Research YIP (N00014-16-1-2540), Wells Fellowship, and UMD Graduate School Summer Research Fellowship.

Table of Contents

List of Tables

List of Figures

List of Abbreviations

CMOS	Complementary-metal–oxide–semiconductor
EDS	Electron density of states
EDX	Energy dispersive X-ray spectroscopy
ENZ	Epsilon near zero
FDTD	Finite difference time domain
HEB	Hot-electron bolometer
LSP	Localized surface plasmon
NIR	Near infrared
NMSE	Normalized mean square error
PML	Perfectly match layer
PVD	Physical vapor deposition
SNOM	Scanning near-field microscopy
SP	Surface plasmon
SPP	Surface plasmon polariton
TM	Transverse magnetic
TMM	Transfer matrix methods
TTM	Two-temperature model
UV	Ultraviolet
XRD	X-ray diffraction

List of Publications

- **S. Memarzadeh**, J. Kim, Y. Aytac, T. E. Murphy, J. N. Munday, "Surface plasmon assisted control of hot-electron relaxation time", Optica 7(6), 608-612 (2020).
- **S. Memarzadeh**, K. J. Palm, T. E. Murphy, J. N. Munday, "Control of hot-carrier relaxation time in Au-Ag thin films through alloying", Optics Express, 28, 33528-33537 (2020).
- T. Gong, P. Lyu, K. J. Palm, **S. Memarzadeh**, J. N. Munday, and M. S. Leite, "Emergent Opportunities with Metallic Alloys: From Material Design to Optical Devices", Advanced Optical Materials, 2001082, 1-21 (2020).

Chapter 1: Introduction

1.1 Motivation

Absorption of incident photons within a conductive material can result in the generation of highly energetic, non-thermal carriers, also known as "hot-carriers". In recent years, generation of photo-excited hot-carriers has been extensively investigated for applications such as photodetection in NIR [1, 2], hot-electron bolometer (HEB) [3, 4], photothermoelectric effects in graphene for THz detection [5, 6], photocatalysis for deriving chemical reactions such as in artificial photosynthesis [7], and water splitting [8, 9]. However, the efficiency of the hot-carrier-based devices used in the aforementioned applications extensively relies on the generated hot-carriers' temporal dynamics. Thus, understanding the temporal response of the hot-carriers can improve the design of hot-carrier devices. For example, a significant amount of the incident solar energy in solar cells dissipates quickly due to the rapid decay of generated hot-carriers, which is not converted to usable electric energy in traditional photovoltaic cells. This process limits the harvest of the hot-carriers and results in low power conversion efficiency. By comparison, hot-carrier solar cells can, in principle, be much more efficient with theoretical values of 66% for unconcentrated sunlight, and ($\sim 85\%$) at the maximum concentration (46,200 suns) [10].

The main goal of this dissertation is to search for new approaches to control the relaxation time of excited hot-carriers. For this purpose, we utilize an ultrafast time-resolved spectroscopy method to measure the ultrafast response of the excited hot-carriers.

1.2 Surface plasmons

Surface plasmons (SP) are the coherent oscillations of electrons at the interface between two materials, typically metal and dielectric, with different signs in their dielectric functions. Compared to the incident photons, SPs are shorter in wavelength, more tightly confined spatially, and have a higher field intensity. Generally, surface plasmons are divided into two classes: localized surface plasmons (LSPs) and surface plasmon polaritons (SPPs), with the dispersion relation expressed as [11]

$$k_{sp} = k_0 \left(\frac{\epsilon_d \epsilon_m}{\epsilon_d + \epsilon_m} \right)^{1/2}, \tag{1.1}$$

where k_0 is the wave vector in free space, ϵ_d is the permitivitty of the dielectric material, and ϵ_m is the metal dielectric function. For LSPs, the incident photons interact with a conductive nano-structure, leading to strong local fields rather than propagation. For SPPs, once the light couples into the surface plasmons mode, it propagates on the metal-dielectric interface and attenuates after a propagation distance of [11]

$$\delta_{sp} = \frac{1}{2k''_{sp}} = \frac{c}{\omega} \left(\frac{\epsilon'_m + \epsilon_d}{\epsilon'_m \epsilon_d} \right)^{3/2} \frac{(\epsilon'_m)^2}{\epsilon''_m} \tag{1.2}$$

with k''_{spp} defined as the imaginary part of the complex surface plasmon wave vector, ϵ'_m as the real and ϵ''_m imaginary part of the dielectric function of the metal, and ϵ_d as the permittivity of the dielectric material. SPPs are surface waves with electromagnetic fields that are evanescent on both sides of the metal/dielectric interface. The surface plasmon propagation distance for gold at 700 nm wavelength is about 5 μm. They are excited under certain conditions (i.e., specific incident energy for a particular incident angle), which satisfy the momentum matching between the incident photons and the propagating SPP. Surface plasmons have applications in biomolecular studies and biosensors [12, 13], imaging [14], and spectroscopy [15]. In addition, they are several excellent review articles and books [16, 17, 18, 19, 20].

1.2.1 Methods of SPP excitation

In 1902, Wood made the first observation of the surface plasmon resonance through the uneven spectrum of the diffracted light reflected from a metallic diffraction grating [21]. Otto then demonstrated that the drop in the reflectivity from the attenuated total reflection (ATR) method in a silver film in close proximity to a prism was due to surface plasmon coupling [22]. In 1968, Kretschmann proposed another attenuated total reflection method in silver, today known as the Kretschmann configuration (or prism coupling technique), which resulted in a similar drop in the reflectivity due to surface plasmon coupling in a silver coated prism [23]. Both Otto and Kretschmann configurations enable coupling through a high index dielectric prism. This material enables the increase in the wave vector of the incident light

to match with the SPP wave vector. The only difference in the Otto configuration is light first tunnels within a small dielectric gap (air) before reaching the SPP mode. A complementary approach to excite the SPPs can be made by decreasing the SPP wave vector by replacing a typical dielectric at the metal/dielectric interface with a dielectric that has a real part of the refractive index lower than 1 [24, 25]. This approach results in a prism-free direct coupling to SPPs. There are other approaches besides these conventional methods, such as using a SNOM probe technique or using a grating structure [26, 27]. Throughout this dissertation, we employed the Kretschmann configuration (prism coupling technique) for excitation of the propagating surface plasmons.

1.3 Hot-electron generation with surface plasmon coupling

Electrons that are not in thermal equilibrium with the material's atoms are known as the hot-electrons. In recent years, due to the advancement in nanoscale system designs and fabrication, hot-carrier generation studies have rapidly expanded due to the ease. In such cases, the excited surface plasmons decay either radiatively by emitting photons or non-radiatively through the generation of the energetic electron-hole pairs (i.e., hot-carriers) via Landau damping. This hot-carrier excitation can even be followed by the photoemission process if the excited hot-carrier has higher energy than the work function of the material. In the non-radiative case, the generated electron-hole pairs have higher energy than the carriers closer to the Fermi energy, resulting in a broad distribution of the carriers above the Fermi energy, as

shown schematically in Figure 1.1.

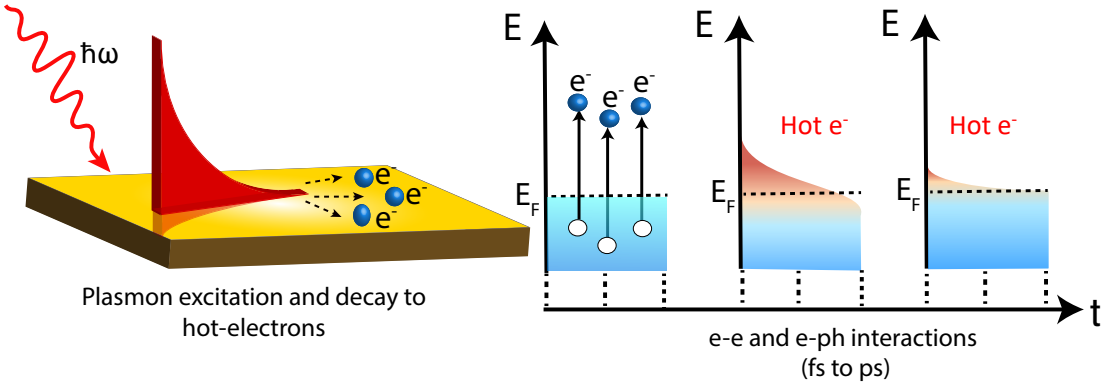

Figure 1.1: Generation of the hot-electrons upon the decay of the propagating surface plasmon in a thin metal film. This decay results in the generation of the excited hot-electrons with a higher temperature than the ambient temperature. Due to the e-e interactions, electrons equilibrate among themselves to a hot-electron distribution which is described by the Fermi distribution. Subsequently, e-ph interactions result in the cooling of the hot-electrons to the lattice temperature.

1.4 Hot-carrier cooling mechanisms

Carrier cooling is a multistep process. In a nanostructured plasmonic system, this cooling occurs first by plasmon dephasing, which happens on the order of 10s of femtosecond. The next step is the inelastic electron-electron scattering, typically in the order of 100s of femtoseconds. The third step, which happens in a longer time scale, typically on several picoseconds, is the process of carriers scattering with phonons (electron-phonon scattering). The optical phonons emitted by the excited carriers then interact with other phonons, which may decay into a low energy acoustic phonon and result in heat dissipation, which occurs in 10-100 ps [17, 28]. Energy dissipation to the surrounding medium occurs via phonon-phonon coupling and induces high local temperatures that can destroy cancerous cells [29]or distill

organic solvents[30].

Ultrafast transient transmission or reflection spectroscopy is an effective tool to study the hot-carrier cooling dynamics. Previous studies have been performed on the ultrafast dynamics of noble metal films [31], single nanoparticles, and ensembles. For example, Hu *et al.* showed that the rate of energy dissipation in Au nanoparticles depends on their size; smaller particles have faster relaxation time [32]. Zijlstra *et al.* presented the first acoustic vibration measurements of a single gold nanorod with an average size of 90 nm $\times$ 30 nm using pump-probe spectroscopy [33]. Ultrafast temporal dynamic studies are not only limited to the noble metals. Other materials, such as aluminum nanostructures have gained a lot of interest for hot-carrier studies because of their low cost, abundance, CMOS compatibility, and capability of supporting tunable resonances that span the entire visible spectrum. Su *et al.* found that, unlike the gold nanostructures, the ultrafast optical response of aluminum nanodisks is more sensitive to the lattice temperature than the electron temperature [34]. Li *et al.* observed a hot-carrier cooling lifetime as slow as 32 ps in perovskite nanocrystals; that is much longer than those reported for other semiconductor bulk or nanomaterials (e.g., for GaAs thin films, the reported hot-carrier cooling lifetime is about 2 ps)[35].

1.5 Dissertation outline

This dissertation is divided into six chapters. The first chapter is the introduction and background information. Chapter 2 discusses the details of the experimen-

tal setup developed for the hot-carrier relaxation time measurement. Chapters 3, 4, and 5 cover the effect of propagating surface plasmons and metallic alloys as the two studied external factors to control the relaxation dynamics of excited hot-carriers. Final thoughts and future work is discussed in Chapter 6.

Chapter 2: Experimental method for hot-electron relaxation time measurements

2.1 Overview

Many processes, including the molecular vibration, emission and absorption of photons, and scattering phenomena, take place in a very fast time scale. Some of them may occur as fast as a femtosecond (10^{-15}s) temporal range. While these phenomena are too fast to be observed using conventional cameras or detectors, one can employ ultrafast lasers to stimulate and probe the response of materials with femtosecond resolution, which leads to a better understanding of the physics of light-matter interactions. In this chapter, we discuss the design of our experimental setup in detail. We also include some of our measurements in this chapter for completeness.

2.2 Experimental setup

The purpose of time-resolved pump-probe spectroscopy is to measure the changes in the reflectivity or transmission of a lower power "probe" pulse induced from a high-power "pump" pulse as a function of the time delay between the two.

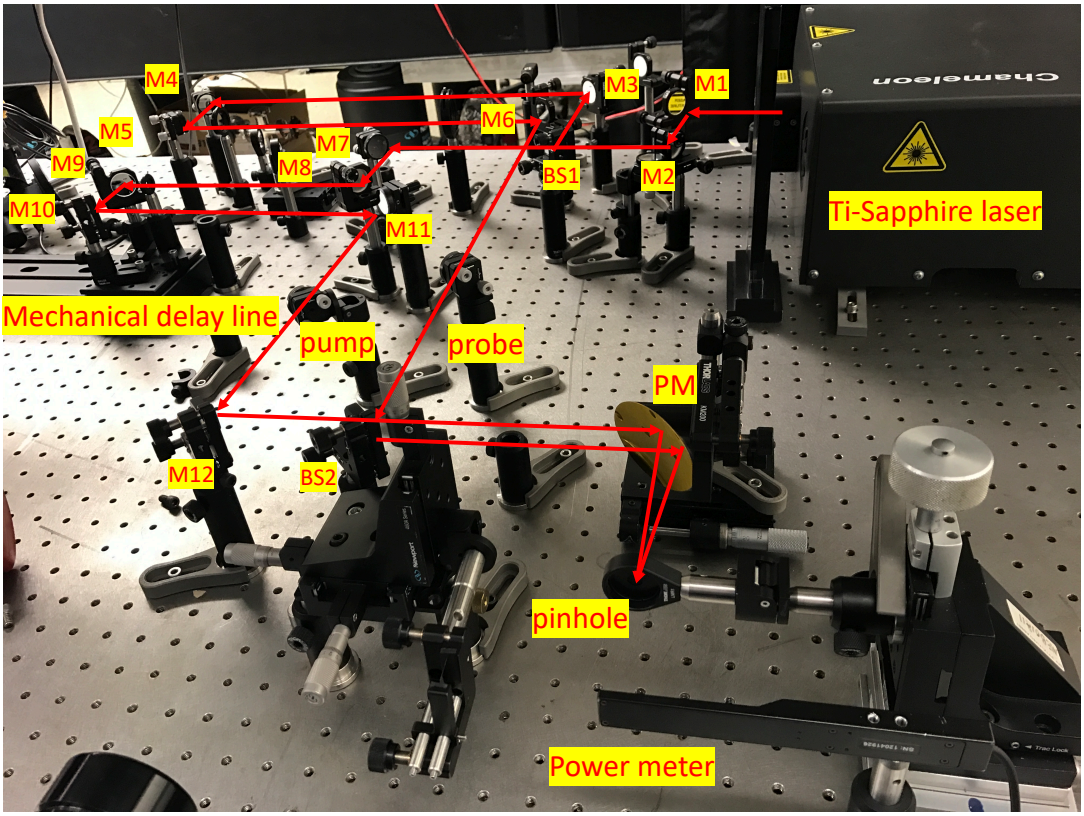

Figure 2.1: Experimental setup of the pump-probe measurement.

These changes in the differential reflectivity measurements of the probe exhibit themselves in the form of:

$$\frac{\Delta R(\tau)}{R} = \frac{R_{\text{with pump}} - R_{\text{w/o pump}}}{R_{\text{w/o pump}}} \tag{2.1}$$

Our laser source is an ultrafast Ti-Sapphire ($Ti : Al_2O_3$) pulsed laser with an 80 MHz repetition rate, tunable between 680 nm to 1060 nm. In this setup, shown in Figure 2.1, the Ti-Sapphire output separates into pump and probe paths right after the beam splitter (BS1). The pump beam is then sent to a mechanical delay line and modulated by an optical chopper with 600 Hz frequency. The lock-in amplifier is synchronized with the frequency of the chopper and captures the

transient change in the probe beam reflectivity. Furthermore, both pump and probe pulses need to overlap in space and coincide in time when they reach the sample. According to the Ti-Sapphire specification, the output of the laser is p-polarized (TM); however, still, linear polarizers are placed in the path of both beams to make them fully polarized. We also measured the laser pulse width by directing a portion of the beam to the APE autocorrelator. The result of this measurement is shown in Figure 2.2. Gaussian fit to the recorded data demonstrates a pulse width of ∼150 fs at 800 nm.

The measurements are performed over ∼6 ps delay time produced by moving the mechanical delay stage for 1mm. The final measurements are reported after scanning the delay line multiple times and averaging the time traces. The laser average power at 800 nm is 3.2 W, and the pump power is measured ∼630 mW right before the sample. Figure 2.3 shows the full pump power spectrum at the same position right before the sample.

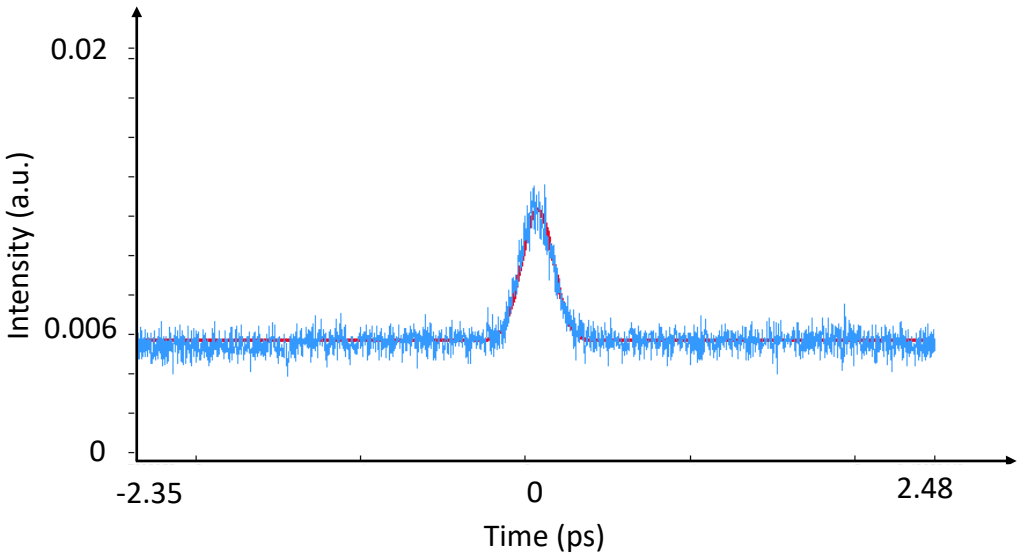

Figure 2.2: Pump pulse width measured with an autocorrelator. The Gaussian fit shows the pulse width of 150 fs.

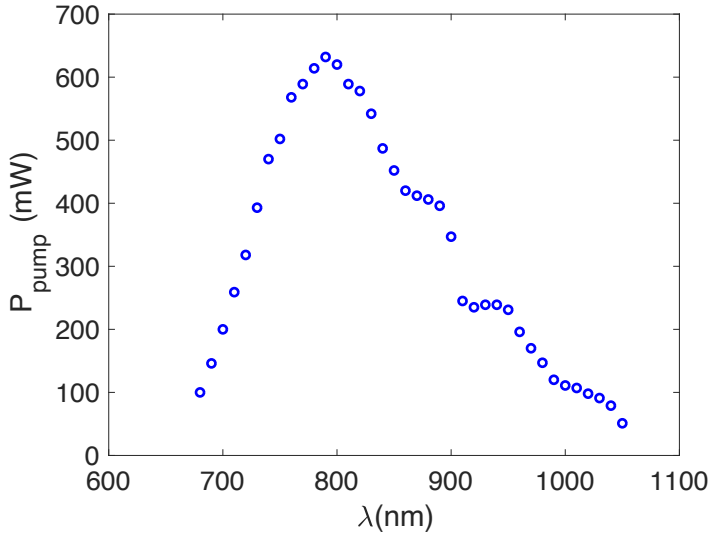

Figure 2.3: Pump power spectrum measured after parabolic mirror and before the sample.

2.3 Spot size measurement

The main challenge in designing the pump-probe optical setup is the spatial and temporal overlapping of the two beams at the sample surface. A 20-micron pinhole size is used to overlap the two beams spatially. These beams are first aligned entirely parallel to each other and directed vertically to a gold-coated parabolic mirror. The pinhole position is then adjusted using a 3D translational stage to maximize the light transmitted through the pinhole. The ratio of the intensity before and after the pinhole can be used to estimate the spot size and can be computed based on the Gaussian beam profile assumption [36] as follows:

$$E(r) = E_0 e^{-r^2/w_0^2} \tag{2.2}$$

Where E_0 is the normalized field and w_0 is the radius at which the amplitude drops to the $1/e$ of the peak value. The intensity is also Gaussian and is expressed as follow,

$$I(r) = I_0 e^{-\frac{2r^2}{w_0}} \tag{2.3}$$

The intensity before (I_{before}) and after (I_{after}) the pinhole can be calculated by taking an integral from the above equation,

$$I_{\text{before}} = \int_0^{\infty} I_0 e^{-\frac{2r^2}{w_0}} 2\pi r dr = \frac{\pi w_0^2}{2} \tag{2.4}$$

$$I_{\text{after}} = \int_0^{d/2} I_0 e^{-\frac{2r^2}{w_0}} 2\pi r dr = \frac{\pi w_0^2}{2}(1 - e^{-d^2/2w_0^2}) \tag{2.5}$$

Here d is the diameter of the pinhole. Thus, spot size (w_0) can be obtained using the following equation

$$\frac{I_{\text{after}}}{I_{\text{before}}} = 1 - e^{-\frac{d^2}{2w_0^2}}. \tag{2.6}$$

2.4 Pump-probe measurement procedure

Once the two beams overlap and the smallest spot size is acquired by adjusting the pinhole's position, we remove the pinhole and place the prism at the same place. The prism location is controlled by moving a 3D stage, and the overlap of the two-beam is confirmed using a microscope objective with a AmScope MU1000 digital camera. Figure (2.4) shows our experimental setup when the prism is replaced instead of the pinhole. The prism is also located on a rotational stage to adjust the surface plasmon coupling's incident angle. Both rotational stage and mechanical delay line are controlled with LabVIEW (National Instruments) software. As both pump and probe beams are p-polarized and collide on the gold-coated prism's surface with a small incident angle difference, both beams contribute to the propagating surface plasmons. However, the final angle is adjusted to the probe beam coupling, that results in a minimum reflected signal. The reflected probe beam is then directed to the silicon photodetector, and its output is fed into the lock-in amplifier.

Measurements of the surface plasmon linewidth and the laser spectral width are shown in Fig. (2.5). We then measured the pump-probe signal from a 50 nm gold-coated prism by manually sweeping the wavelength from 680 nm to 720 nm

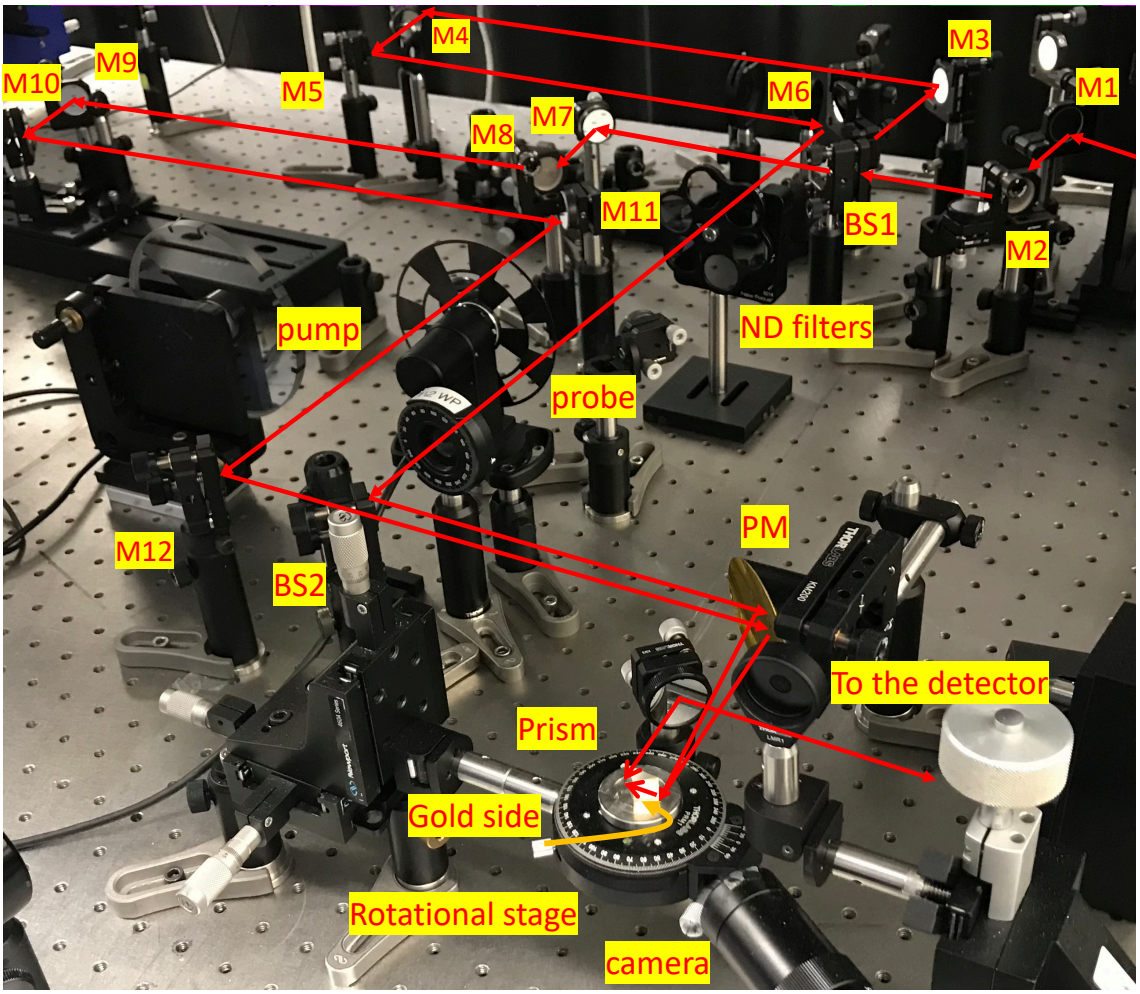

Figure 2.4: Experimental setup with a gold-coated prism.

with a 5 nm increment under the fixed pump power (Figure (2.6)). Here, the prism position is adjusted to have the maximum surface plasmon coupling at 700 nm. The wavelength adjustment happens through an external laser knob and is confirmed with the manufacturer software, connected to the built-in laser spectrometer via a USB. The full-width half maximum of the captured reflectivity signal for the 50 nm Au film deposited on a prim is ∼50 nm, and out of this range, the signal almost vanishes. For these measurements, the pump power is set to 200 mW and the probe power is 20 mW.

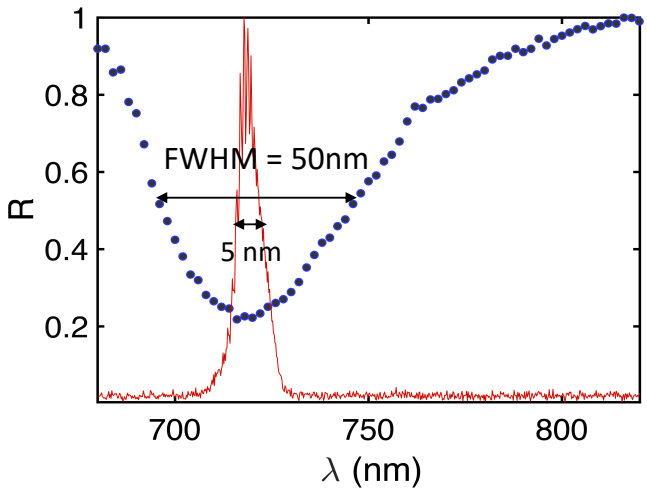

Figure 2.5: Plasmon linewidth measurement for a 50 nm gold film (blue dots) and the spectral measurement of the Ti-Sapphire laser (red line).

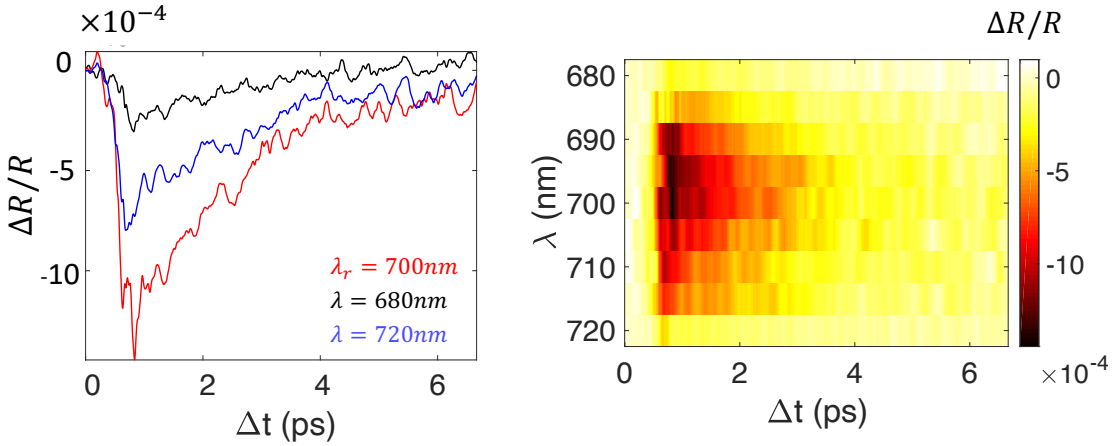

Figure 2.6: Pump-probe signals recorded for a 50 nm Au film deposited on a right angle prism while coupled to the propagating surface plasmon at 700 nm wavelength.

2.5 Polarization dependence of degenerate pump-probe signal

Only the p-polarized waves will couple to the surface plasmon, and so adjusting the polarization will affect whether the surface plasmon is excited. Thus, we placed a half-wave plate in front of each beam to investigate the pump polarization dependency and probe measurements on the transient reflectivity signal. The half-

wave plate controls the pump polarization from fully p to s polarized beam. For this measurement ($\lambda_{pump} = \lambda_{probe} = 725$ nm), the pump and probe powers are 224 mW and 3.8 mW, respectively.

Figure (2.7) shows our gold film normalized reflectivity measurements deposited on a right-angle prism upon both pump and probe coupling to the propagating surface plasmon (both p-polarized). Here, we used a manual rotational stage with an angular resolution of 0.2 degrees. According to this figure, the difference between the two beams' coupling angle is $\leqslant 0.2$ degrees at 725 nm. Therefore, it is a reasonable assumption to consider that both beams couple to the propagating surface plasmon under approximately the same coupling angle.

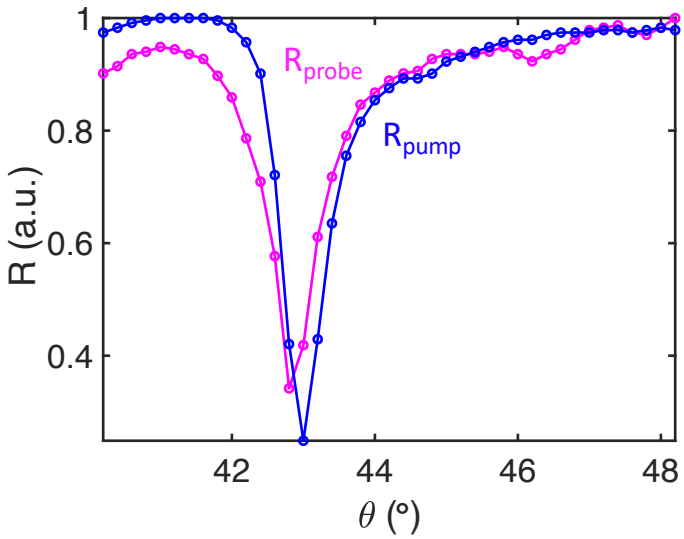

Figure 2.7: Coupling to the propagating surface plasmon of a 50 nm Au film under the Kretschmann configuration using both pump and probe beams.

Under the resonance angle, the differential reflectivity signal is recorded for both p and s polarized pump beam while keeping the probe beam polarization unchanged (p-polarization). Figure 2.8 illustrates the captured signal for such mea-

surements. The recorded signal is then fitted with double exponential function; the result of the longer decay which is due to the electron-phonon interactions are $\tau_p = 1.62 \pm 0.19ps$ and $\tau_s = 1.40 \pm 0.14ps$, respectively. Here, τ_p and τ_s are the relaxation time of the p and s-polarized pump beam. The hot-electron relaxation time varies ∼0.2 ps by changing the pump polarization direction. Also, the amplitude of the recorded signal reduced significantly (∼10 times smaller), as depicted in Fig. (2.8). Furthermore, we observed that the probe beam decoupling due to the polarization change results in no pump-probe signal in our measurements' sensitivity range.

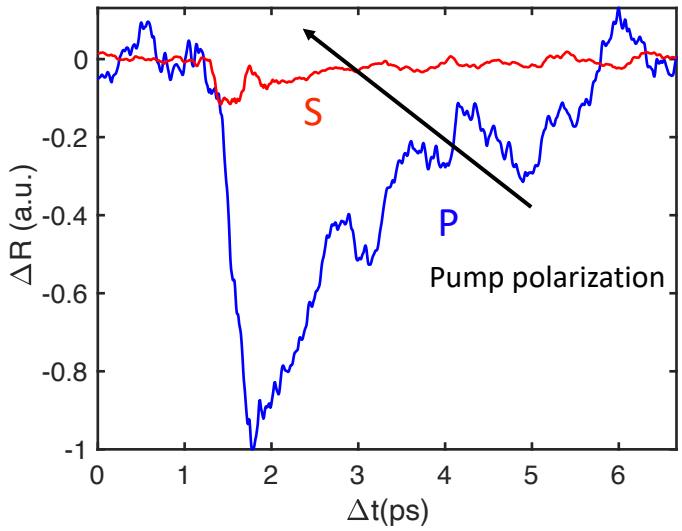

Figure 2.8: Polarization dependence of the pump-probe differential reflectivity signal for a 50 nm gold film deposited on a right angle prism. The resonance wavelength is 725 nm.

2.6 Conclusion

In summary, we discussed the experimental design of our degenerate pump-probe set up. We incorporated the surface plasmon coupling stage into our pump-probe setup to enhance the signal amplitude. In the next chapter, we examine the effect of the surface plasmon coupling on the hot-electron relaxation time.

Chapter 3: Surface plasmon assisted control of hot-electron relaxation time

3.1 Overview

In the previous chapter, we discussed the detail of our pump-probe experimental design. This chapter focuses on incorporating the propagating surface plasmon with our pump-probe measurements and investigating its importance on the hot-electrons relaxation time.

3.2 Introduction

Recently, the optical generation of hot-carriers in metallic components has attracted interest for applications such as solar energy conversion [37, 38, 39, 40, 41], non-linear optics [42, 43, 44], sensitive photodetectors [45, 46, 47, 48], nanoscale heat sources [49], photochemical reactions in biomolecular studies [50, 51, 52], and biosensors [53, 54]. For the excitation of hot-carriers in metals, the incident photon energy is typically lower than the energy of the band-to-band transition, thus the efficiency of hot-carrier generation is reduced as a result of the poor absorption of light within the metals. To overcome this limitation, surface plasmons have been

broadly utilized to enhance absorption through the use of metallic nanostructures [55, 56, 57, 58, 59], which increase the measurement sensitivity because of the increased absorption [60].

As we discussed in chapter 1, hot-carriers relax to equilibrium through plasmon dephasing via Landau damping, electron-electron (e-e) scattering, electron-phonon (e-ph) scattering, and lattice heat dissipation through phonon-phonon (ph-ph) interactions [61]. Throughout these processes, hot-carriers can distribute their energy to the surrounding environment and in turn thermalize from their excited state to equilibrium. The temporal duration of hot-carrier relaxation is the key factor to determine the performance of hot-carrier devices. For example, the efficiency of hot-carrier injection in energy conversion systems [41, 62] and the operating speed in optical modulation systems [63, 64] are both strongly linked to hot -carriers' lifetime. Depending on the geometry of metal nanostructures, the materials' band structure, and the incident photons' energy [57], the relaxation time can vary from a few hundred femtoseconds up to a couple of picoseconds. In the case of gold and aluminum nanostructures, relaxation times on the order of hundreds of picoseconds, due to the acoustic vibrations of the lattice, have been reported [65, 66, 67]. The effect of enhanced absorption on hot-carrier relaxation time has been extensively studied in the case of the thin film and nano-structured plasmonic systems [68, 69, 70]; however, the importance of the strongly confined field inside the metal thin film induced by surface plasmon coupling on hot-carrier lifetimes is still elusive. Transient reflectivity measurements using pump-probe spectroscopy are a common method to characterize carrier dynamics under the intra-band or inter-band tran-

sitions. Typically, the measured transient signals for pump-probe spectroscopy are analyzed with the Two-Temperature Model (TTM), which describes the spatiotemporal profile of the electron and the lattice temperature from a coupled nonlinear partial differential equation [71, 72, 73]. This model is very useful in understanding relaxation dynamics, but appropriate modification is needed for an accurate modeling of the unique internal electric field profile in metal films due to its coupling to the propagating surface plasmon.

In this chapter, we experimentally investigate the relationship between the hot-carrier relaxation time and the characteristics of surface plasmons on gold (Au) thin films excited under the Kretschmann configuration. For accurate theoretical modeling of the transient reflectivity data resulting from the carrier dynamics in the conduction band of Au thin film, we employ the free electron model to estimate the elevated electron temperature due to intra-band optical pumping. From the calculated electron temperature, we extract the carrier relaxation time with the modified TTM to better describe the localized electric field distribution inside the Au thin film. Under fixed absorbed power in the Au film over the spectral range of 730 nm to 775 nm (resonance wavelength at 745 nm), we observe that the hot-electron relaxation time in the Au film reaches its maximum at the resonance wavelength, which indicates that the modified intensity and profile of the internal electric field by the excitation of surface plasmons plays a significant role in hot-carrier relaxation.

3.3 Experimental and numerical measurements of SPP excitation in Au

For experimental measurements, we use a precise motorized rotational mount with 25 arcsecond angular resolution to couple to the propagating surface plasmon under the Kretschmann configuration (Fig. 3.1a). The incoming beam from the glass interface is focused on the Au side of the prism using an off-axis parabolic mirror. Both reflection and transmission are recorded while rotating the prism on the stage. Transmission of the gold film is measured to be less than 1% and, therefore, negligible for determining the absorption ($A = 1 - R$) measurement. We optimize our absorption measurement using a bare prism first, without any Au coating, to incorporate the possible scattering effects from every prism interface. This helps to measure the baseline of the reflection signal. For the range of angles and wavelengths employed, the bare prism exhibits total internal reflection at 45 degrees. The Au-coated prism then replaces the bare prism on the rotational stage for the surface plasmon coupling. The reflection signal is recorded over the incident angle for the various pump wavelengths. The final reported signal is the ratio between the reflectivity measured using the gold-coated and uncoated prisms (Fig. 3.2b).

We employ the transfer matrix method for the numerical calculation of absorption (Fig. 3.2a). The thickness of the Au film and the incident angle of light are set to 44 nm and 44°, respectively. Under these conditions, surface plasmon excitation

occurs at 745 nm (1.66 eV), where the photon energy is lower than the d-band transition of Au, at 2.4 eV [74]. Once the surface plasmon is excited in the Au film, the electric field is strongly confined at the interface between the Au film and air. Figure 3.1b shows absorption as a function of wavelength ranging from 730 nm to 775 nm, with resonance wavelength at 745 nm. Coupling to the propagating surface plasmon results in the maximum absorption of 85%. The numerical (solid line) and experimental results (dots) of the absorption spectrum in a broader range (from 700 nm to 800 nm) are shown in Figure 3.2c.

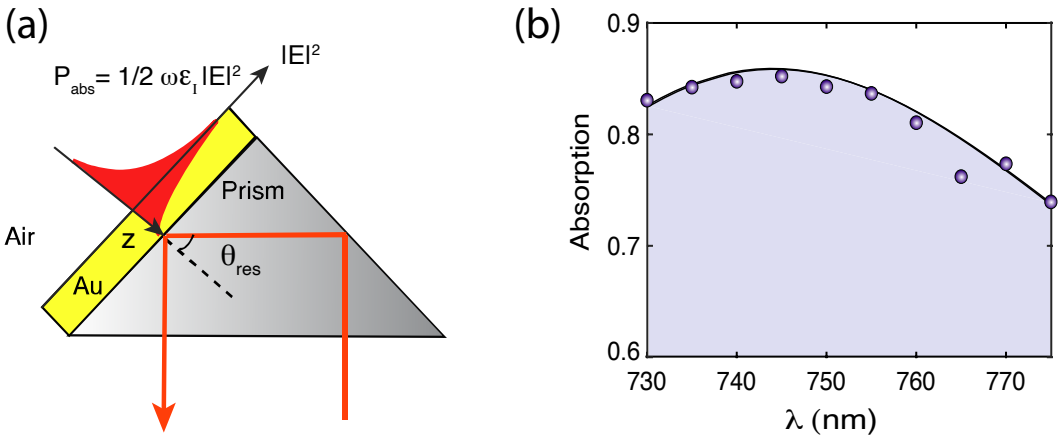

Figure 3.1: (a) Schematic of light coupling to propagating surface plasmons using the Kretschmann configuration. (b) Absorption measurement (circles) and simulation (solid line) after surface plasmon coupling.

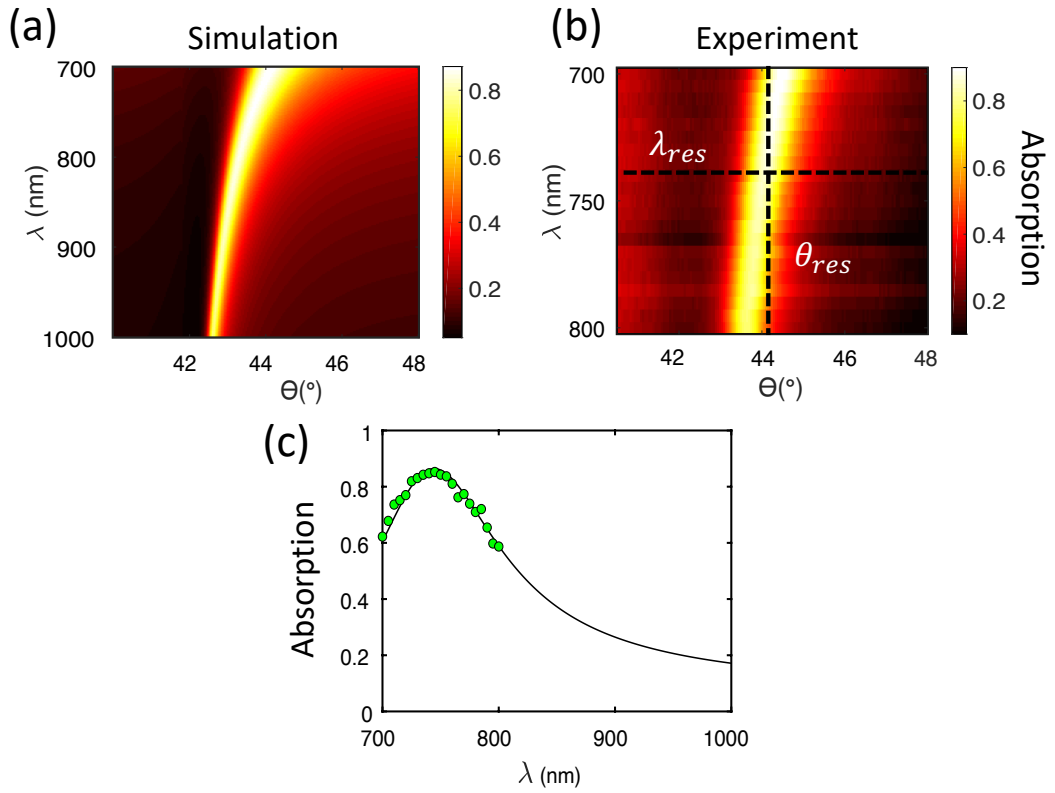

Figure 3.2: (a) Simulation and (b) measurement absorption for the gold sample while coupling to the propagating surface plasmon for different incident wavelengths. In (c), the solid line (simulation) and dots (experiment) are extracted from the computed mesh plots in (a) and (b) at 745 nm resonance wavelength, respectively.

3.4 Experimental procedure

As discussed in chapter 2, we utilize a degenerate pump-probe technique for the time-resolved differential reflectivity measurements, once coupled to the propagating surface plasmon of gold at 745 nm resonance wavelength. The simplified schematic of the setup is shown in Fig. 3.3. Here, transverse-magnetic (TM) polarized pulses are produced from a femtosecond high-power Ti-Sapphire laser with an 80 MHZ repetition rate. Using a beam splitter, the incoming pulses are then separated into pump and probe paths. Both beams are directed to coincide on the gold surface after

reflecting off the off-axis parabolic mirror to a spot size of approximately 40 μm. After spatially separating the two beams, the probe beam is then directed to the Si photodetector for differential reflectivity measurements. The time delay between the pump and probe pulses are produced by passing the pump beam through the mechanical delay stage.

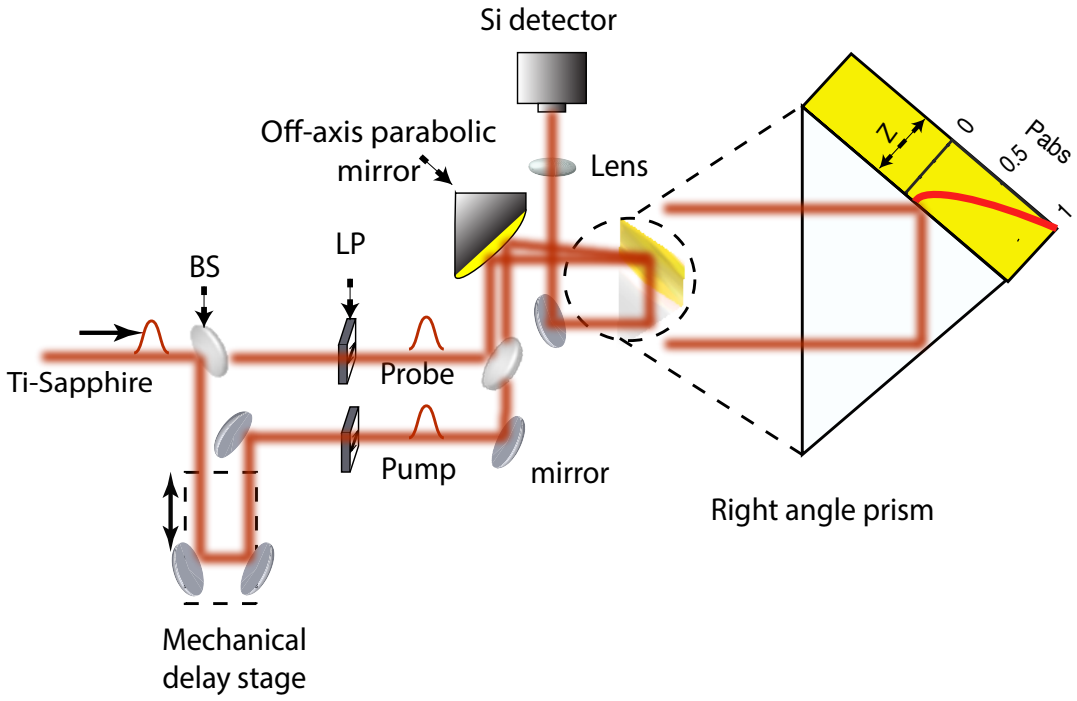

Figure 3.3: Schematic of the pump-probe experimental setup.

To rule out the effect of absorbed light power in the control of the hot-carrier relaxation temporal dynamics, we designed two different experimental conditions:

1) sweeping the wavelength ($\lambda = 730 \sim 775$ nm) with the fixed absorbed power (P_{abs}=120 mW),

2) varying the absorbed laser power (P_{abs}=50 $\sim$ 150 mW) with the fixed wavelength (λ=745 nm).

Figure 3.4a and 3.4b schematically illustrate hot-electron excitation under these two conditions.

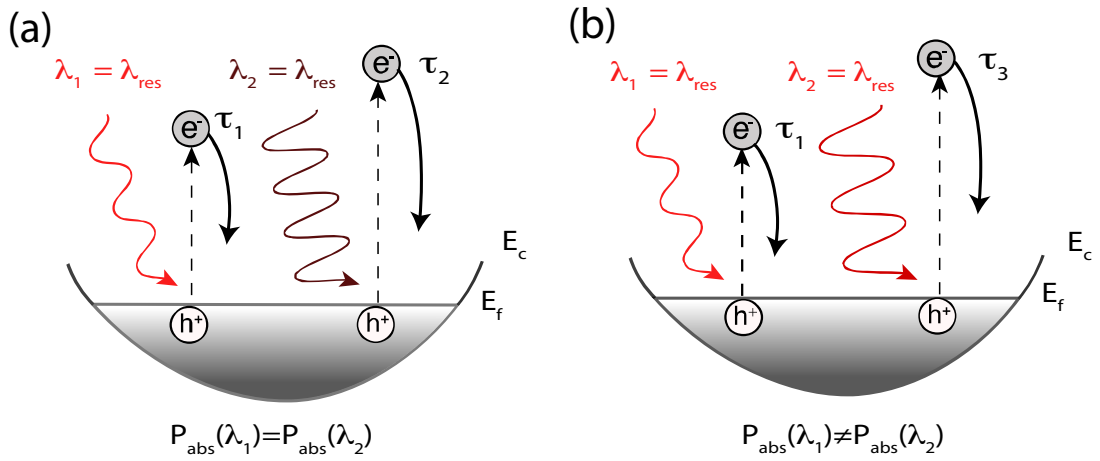

Figure 3.4: (a) Schematic diagram showing hot-electron excitation under resonance and off-resonance wavelengths while keeping the absorbed power fixed (120 mW) for both illuminations. (b) Schematic diagram showing a second case where the hot-electron excitation occurs under the same resonance wavelength (745 nm) but with different absorbed powers. τ_1, τ_2 and τ_3 are the corresponding electron-phonon relaxation time for these different cases.

Transient reflectivity ($\Delta R/R_0$) measurements as a function of time delay (Δt) between the pump and probe for both conditions are shown in Figure 3.5. When the wavelength was varied, we adjust the incident pump intensity according to the absorption spectra (Fig. 3.1b to ensure that the absorbed power remains the same over the entire incident wavelength range. We observe that the transient reflectivity ($\Delta R/R_0$) reaches the maximum at resonance, and signal modulation is gradually reduced as the wavelengths tend away from resonance. For the case of fixed wavelength illumination, the input power is varied (59 mW, 105 mW, 141 mW and 176 mW) at the resonance wavelength.

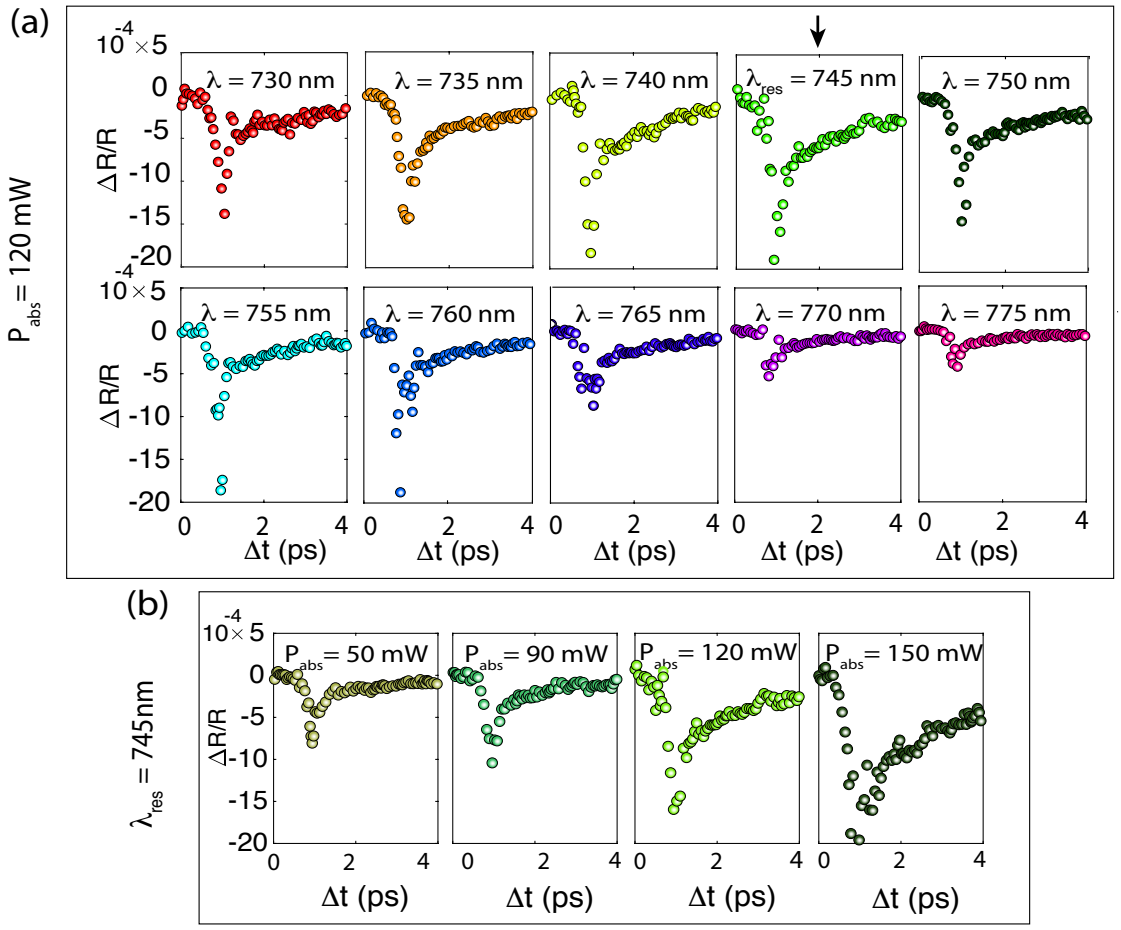

Figure 3.5: (a) Relative reflectivity change for different incident wavelengths ranging from 730 nm to 775 nm measured at fixed absorbed power (120 mW). Resonance wavelength is distinguished by a green frame from the rest of the wavelengths. (b) Relative reflectivity signals under the fixed 745 nm resonance wavelength measured with the different absorbed powers (50 mW, 90 mW, 120 mW, 150 mW).

3.5 Hot-electron relaxation time analysis

To extract the hot-electron relaxation time, we develop a model using a combination of the free electron and modified two-temperature models. Our model is based on converting the transient reflectivity measurements ($\Delta R/R_0$) to electrons temperature under the intra-band optical pumping assumption, which results in a non-equilibrium hot electron distribution that can modify the optical properties of the Au film. The Au band structure is modelled using a simplified parabolic electron density of states [75].

Considering that the carrier density is a temperature independent quantity and the intra-band excitation does not generate extra carriers in the conduction band ($N_{e_{pump}}$=$N_{e_{nopump}}$= 4.92×10^{22} cm^{-3}), we can calculate the Drude plasma frequency ($\omega_p = \sqrt{(e^2 N_e)/(\epsilon_0 m)}$) and damping coefficient ($\gamma_p = \hbar e/(m\mu_e)$) as a function of the electron temperature (detail in the following section). Here, N_e is the carrier concentration, $\epsilon_0 = 8.854 \times 10^{-12}$ F/m is the permitivity of free space, m is the dimensionless effective electron mass, and μ_e is the electron mobility. Figure 3.6 shows the dependency of the above parameters on electron temperature. Based on our calculation, we obtained the plasma frequency of gold equal to 7.845 eV at room temperature.

As numerically depicted in figure (3.6), and experimentally shown in Reddy *et al.*[76], when the inter-band transition is insignificant, the temperature dependencies of the optical properties are mainly due to the change in the plasma frequency (ω_p), effective mass (m), and Drude damping (γ) parameters. As the temperature is

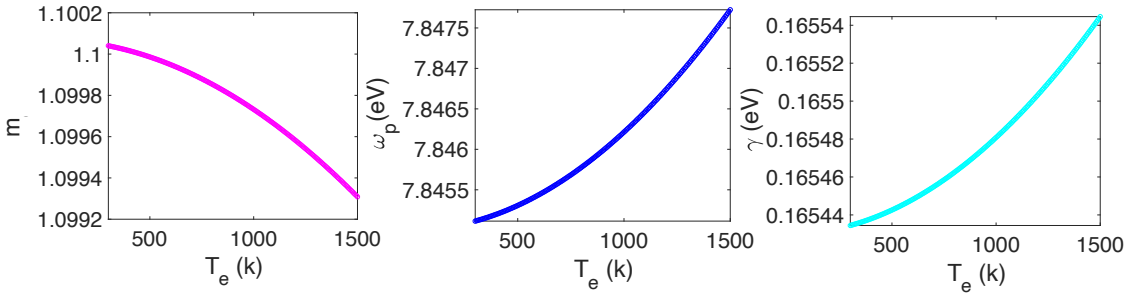

Figure 3.6: From left to right, dependency of the elecctron effective mass, plasma frequency, and Drude damping factor on electron temperature in gold.

raised the effective mass in metals decreases which is in agreement with previous reports [77].

3.5.1 Free electron model

To calculate the changes in the permittivity function due to the intra-band optical pumping, we use a free electron model assuming a parabolic density of states. Starting with a constant value of the carrier density at room temperature, $N_e(T = 300\text{K}) = 4.92 \times 10^{22}(1/\text{cm}^3)$, which is obtained from the ellipsometry fits, using the following equation [78]

$$N_e(T = 300K) = \frac{1}{\pi^2}\int_0^\infty \frac{m_{T=300\text{K}}}{\hbar^2}\left(\frac{2m_{T=300\text{K}}E}{\hbar^2}\right)^{\frac{1}{2}} f_o(\mu_{T=300\text{K}}, T)dE, \qquad (3.1)$$

the chemical potential at room temperature can be computed as $\mu_{T=300\text{K}} = 4.4526\text{eV}$. In the above equation, f_o is the Fermi-Dirac distribution, and $m_{T=300\text{K}} = 1.1\text{eV}$ is the effective electron mass at room temperature.

Under the assumption of a fixed chemical potential level and the same carrier density as for the intra-band optical pumping ($i.e. N_e(T) = N_e(T = 300\text{K})$), we can

implicitly extract the effective electron mass at a higher temperature $m(T)$ from [78]:

$$N_e(T) = \frac{1}{\pi^2}\int_0^\infty \frac{m(T)}{\hbar^2}\left(\frac{2m(T)E}{\hbar^2}\right)^{\frac{1}{2}} f_o(\mu, T)dE. \tag{3.2}$$

Finally, permittivity as a function of the electron temperature can be calculated in terms of the summation between the Drude term (w.r.t to the carrier density (N_e) and mobility (μ) as the fitting parameters) and the Lorentz term according to [79]:

$$\epsilon(\omega, T) = \epsilon_\infty + \frac{-\hbar^2 e^2 N_e \mu_n}{\epsilon_o(\mu_n m(T) + iq\hbar E)} + \sum_n \frac{A_n B_n En_n}{En_n^2 - E^2 - iE.B_n}, \tag{3.3}$$

in which ϵ_∞ is the high-frequency dielectric constant, ϵ_0 is the vacuum dielectric constant, $\hbar$ is the reduced Planck's constant, e is the electron charge, μ is the carrier mobility, A is the amplitude of oscillation, En is the center energy, B is the broadening amplitude, and n is the number of oscillators. Here, the number of oscillators used in the Drude and Lorentz terms are 1 and 2, respectively. All the fitting parameters obtained from the ellipsometry measurement at room temperature are listed in table 3.1.

Parameters	Values
A_1	2.0093
A_2	6.1582
B_1	0.6250 (eV)
B_2	2.8199 (eV)
En_1	2.9580 (eV)
En_2	4.1990 (eV)
μ_1	6.353 ($\frac{cm^2}{V.S}$)
ϵ_∞	3.1990

Table 3.1: **List of the ellipsometry parameters at room temperature.**

Subsequently, the change in the reflectivity with electron temperature over different incident wavelengths can be determined from the above permittivity function and by using the Transfer Matrix Methods (TMM) calculation. According to our numerical modeling, temperature variation causes less than 0.1% variation in the real and imaginary part of the permittivity function (i.e. $\Delta\epsilon_r = 0.03\%$ and $\Delta\epsilon_I = 0.08\%$) (Fig. 3.7).

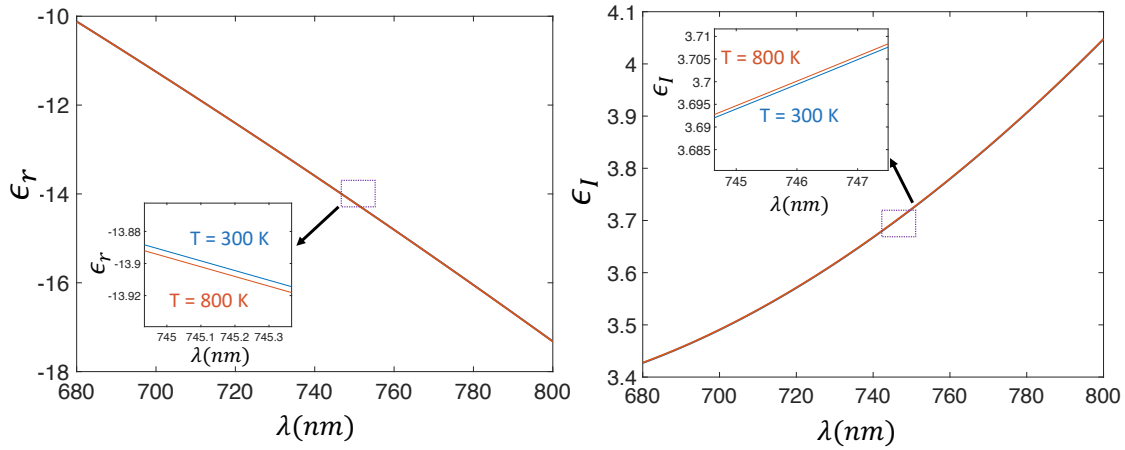

Figure 3.7: Numerically calculated real and imaginary part of the permittivity function at 300 K and 800 K temperature.

3.5.2 Modified two-temperature model

Quantitative theoretical research on modeling the nonequilibrium dynamics started after demonstrating the first generation of the mode-locked lasers in the early 60s. Soon after, and through rapid growth in the femtosecond lasers' applications in material studies, Anisimov *et al.* [72] proposed the conventional Two-Temperature Model (TTM), which describes the interaction of the short lasers pulse with two subsystems, electron and lattice. This model introduces the spatiotemporal (2D) temperature distribution of electron and lattice through solving two coupled non-

linear differential equations. Here, the main difference between the conventional two-temperature model and the modified two-temperature model is that in the second case, the absorbed power profile of the coupled surface plasmon is included in the source term definition of the coupled equations.

The general format of the two-temperature model is as follow:

$$C_e(T_e)\frac{\partial T_e}{\partial t} = K_e\nabla^2 T_e - G(T_e - T_l) + S(z,t) \tag{3.4}$$
$$C_l\frac{\partial T_l}{\partial t} = G(T_e - T_l)$$

where T_e and T_l are electron and lattice temperature [80, 81], $C_e(T_e) = \frac{\pi^2 N_e k_b}{2}(k_b T_e/E_f)$ and $C_l = 2.5 \times 10^6 \mathrm{Jm^{-3}K^{-1}}$ are the electron and lattice heat capacities [80, 82], E_f and k_b are the Fermi level and Boltzmann constant, $K_e = 315\ \mathrm{Wm^{-1}K^{-1}}$ is the electron thermal conductivity, $G = C_e(T_e)/\tau_{e-ph}$ is the electron-phonon coupling coefficient within the weak perturbation approximation with τ_{e-ph} as the electron-phonon relaxation time. Under the weak perturbation regime ($T_e \ll T_f \sim 10^4$), T_f is the Fermi temperature, the electrons' heat capacity is much smaller than the lattice heat capacity; this makes the lattice temperature relatively constant with respect to the electrons' temperature.

Figure 3.8b and 3.8c show the converted electron temperature as a function of time delay for both fixed absorbed power with varied wavelengths, and for fixed resonance wavelength with varied absorbed powers. The converted electron temperatures is modelled using the modified TTM.

In the conventional two temperature model, the skin depth of a material is

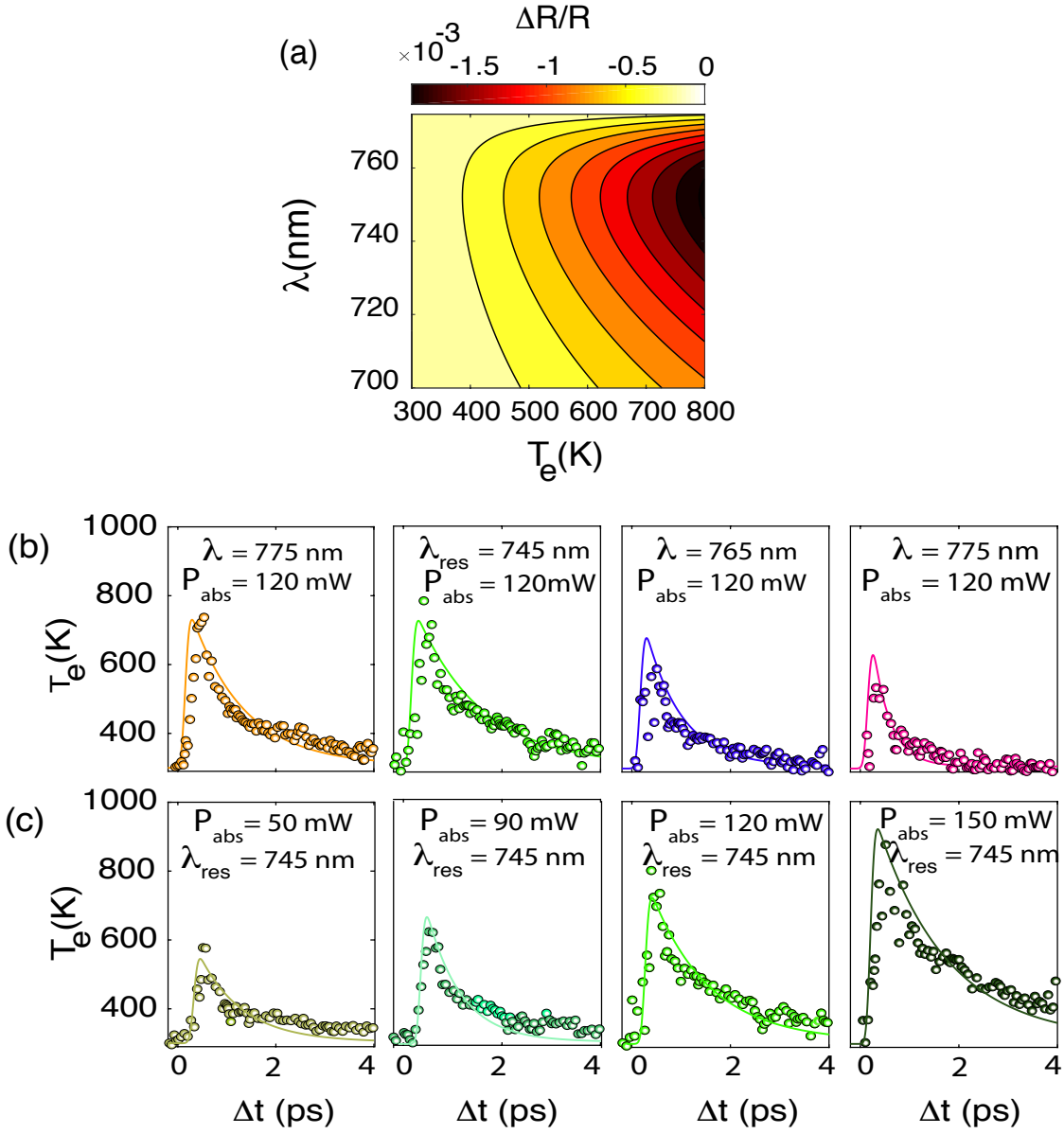

Figure 3.8: (a) Differential reflectivity contour plot computed from the free electron model and transfer matrix methods. Hot-electron temperature as a function of the delay time between pump and probe beams under (b) fixed (120 mW) absorbed power and (c) fixed resonance wavelength (745 nm). The solid lines are the calculated electron temperatures, and the open circles are the electron temperatures obtained from our differential reflectivity measurements.

simply applied to the laser heating source term ($S(z,t)$) to model the laser interaction with the material as a function of depth. Instead, in our modified version, we change the source term by using the decaying length of the confined electric field of the surface plasmon at both sides of the interface instead of skin depth of the Au. Furthermore, using the Finite Difference Time Domain (FDTD) simulation, the electric field profile is numerically computed within the sample throughout the range of the wavelengths. To keep the total absorbed power constant, we vary the input power accordingly. Figure 3.9 shows the results of the normalized electric field profiles over the range of the incident wavelengths. In this figure, the black line corresponds to the electric field profile under no surface plasmon excitations ($\lambda = 745$ nm, $\theta = 0^o$).

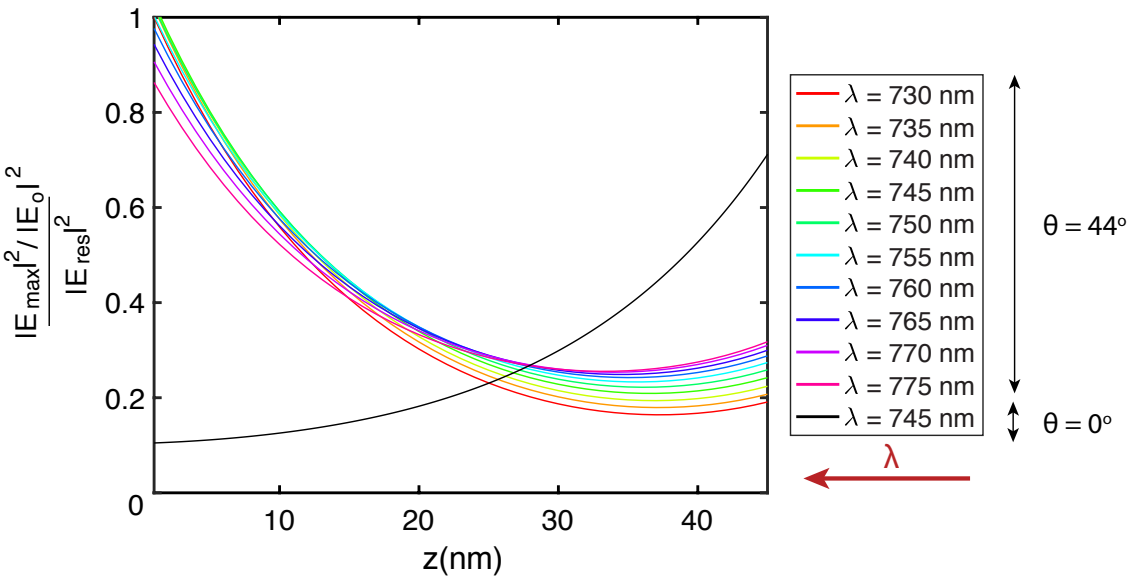

Figure 3.9: Electric field profiles normalized by the intensity of the input field and the electric field at resonance wavelength of 745 nm. Profiles are computed from the FDTD simulation.

The calculated field is fitted with double exponential terms, including the decaying field at the Au/prism interface and the decaying field at the Au/air interface.

The modified source term (S(z,t)) to incorporate the absorbed power profile inside the Au film can be described as:

$$S(z,t) = \sqrt{\frac{\beta}{\pi}}\frac{(1-R)\Phi}{t_p}\left(\frac{a_1}{b_1}e^{-z/b_1} + \frac{a_2}{b_2}e^{(z-d)/b_2}\right)e^{-\beta((t-2t_p)/t_p)^2} \tag{3.5}$$

where $t_p$is the laser pulse width, Φ is the laser fluence, d is the sample thickness and $\beta = 4\ln(2)$ [81]. a_1 and a_2 correspond to the intensity of electric field at Au/air and Au/prism, and b_1 and b_2 correspond to the decaying length of electric field at Au/air and Au/prism, respectively.

Excitation $\lambda(nm)$	a_1	a_2	$b_1(nm)$	$b_2(nm)$
730	0.997	0.137	15.191	12.061
735	1.014	0.149	15.370	13.222
740	1.018	0.163	15.544	14.349
745	1.019	0.179	15.692	15.412
750	1.007	0.195	15.827	16.346
755	0.985	0.210	15.958	17.147
760	0.955	0.224	16.075	17.815
765	0.919	0.236	16.075	18.333
770	0.880	0.248	16.302	18.730
775	0.835	0.257	16.425	19.028

Table 3.2: **Double exponential fitting parameters**

Using our experimental conditions with the modified TTM, we numerically calculate the electron temperature as displayed in Fig. 3.8b and 3.8c. For the case of constant absorbed power, we show four wavelengths and their corresponding best fits on the relaxation time to preserve space. We also incorporate the spatial dependence of the electron temperature by averaging the temperature profiles along the z direction. The result of the fits is shown in Fig. 3.8b and 3.8c based on

the Normalized Minimum Squared Error (NMSE) calculation for the hot-electron relaxation time (Fig. 3.10).

3.5.3 Fitting procedure and error bar calculation

Best fits are selected according to the calculation of the Normalized Mean Square Error (NMSE) between the measured and calculated temperature data obtained from the modified two-temperature model. The fitting parameter is the electron-phonon relaxation time ($\tau_{e-ph} = C_e/G$). Here, the error bars in the hot-electron relaxation time are derived from the 95% confidence bounds calculation on the fitted coefficient. Complete set of the fits for the on- and off-resonance wavelengths are shown in Fig. 3.11.

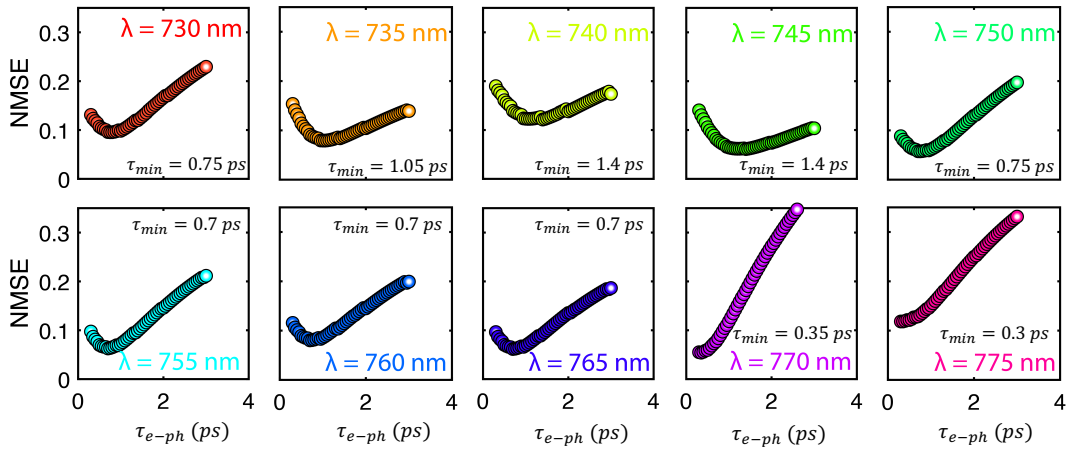

Figure 3.10: NMSE plots for different wavelengths. Resonance wavelength is at 745 nm.

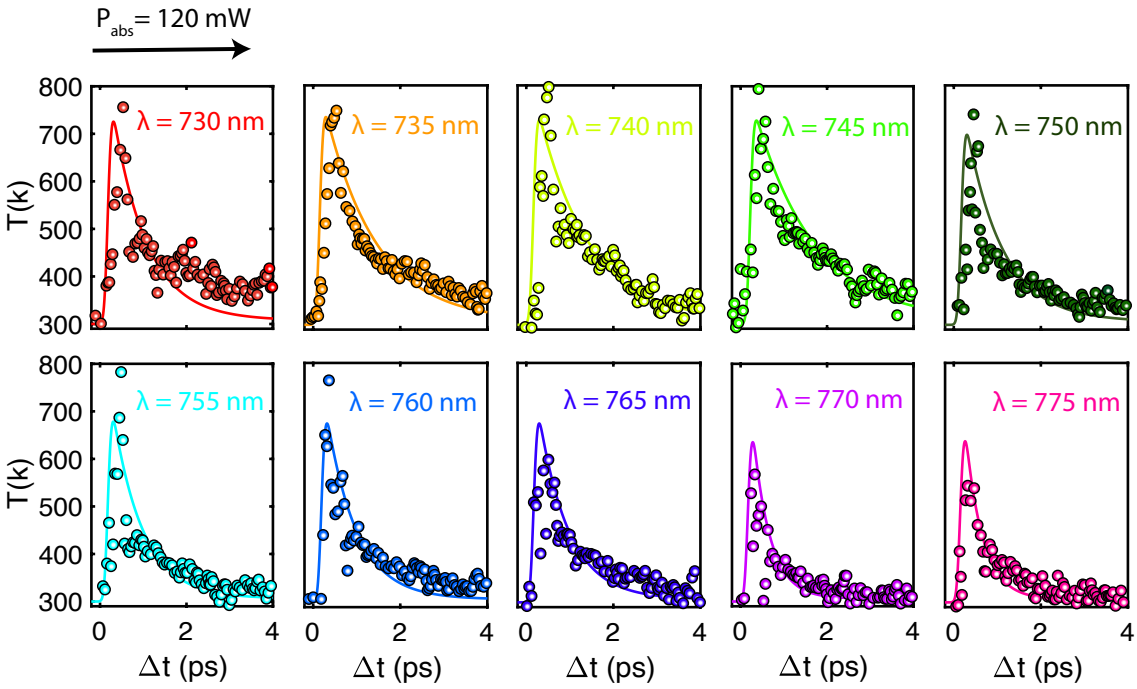

Figure 3.11: Converted pump-probe data to the electron temperature for 10 different wavelengths with their corresponding best two-temperature model fits.

3.6 Effect of electric field enhancement on relaxation time

Figure 3.12a and 3.12b present the extracted hot-carrier relaxation time for both cases of fixed absorbed power and fixed illumination wavelength. When the incident power is varied while coupling to the surface plasmon, the hot-carrier relaxation time increases linearly with increasing incident pump power (Fig. 3.12b). However, when the absorbed power is held constant and the internal field intensity profile is varied (i.e. the amount of surface plasmon coupling is varied), we find that the hot-carrier relaxation time is strongly dependent on the intensity of the electric field (see the trend of hot-carrier relaxation time in Fig. 3.12a and the normalized maximum intensity of electric field in Fig. 3.12c). This result confirms that the surface plasmon coupling can enhance the hot-carrier relaxation time in

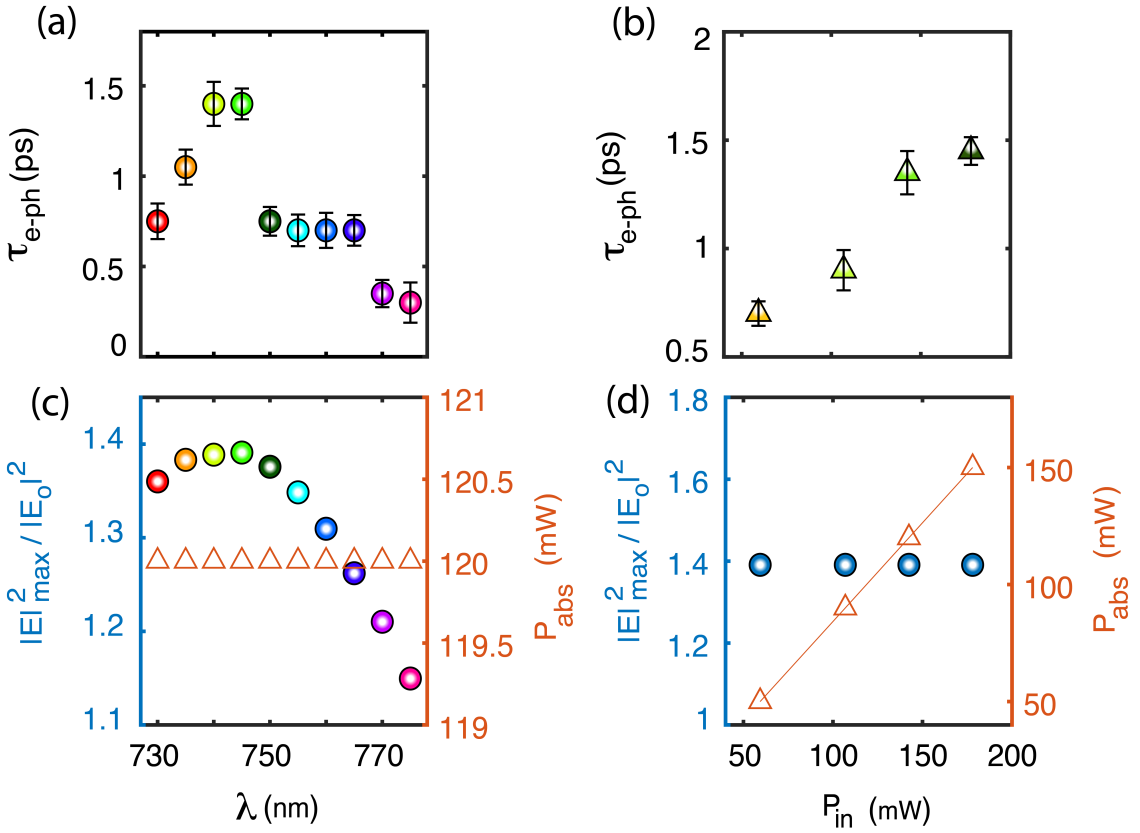

Figure 3.12: Effect of field enhancement on relaxation time due to the surface plasmon coupling under the fixed (120mW) and variable (50 mW, 90 mW, 120 mW, 150 mW) absorbed powers. Experimentally measured hot-electron relaxation time under (a) fixed and (b) variable absorbed powers. Field enhancement computed from the FDTD simulation for wavelengths ranging from 730 nm to 775 nm under the (c) fixed and (d) variable absorbed powers. The electric field profiles are normalized by the intensity of the input field.

the Au film with high field confinement as well as the increase of the light absorption in the Au film. Notably, we can more effectively increase the hot-carrier relaxation time with the local electric field enhancement than with increasing the input power. We achieve approximately a doubling of the hot-carrier relaxation time with only a $\sim$3.5% increase in electric field intensity (normalized to the input field) at the metal/air interface through SP coupling. Although, the hot-electron relaxation time and the corresponding electron-phonon coupling factor have extensively been studied as a function of the elevated electrons' temperature [83, 84], the effect of the electric field confinement on the relaxation time has not fully been determined. Furthermore, we hypothesize that the electric field confinement could affect the reabsorption rate of the non-equilibrium phonon population due to a bottleneck effect. The increase in the reabsorption rate leads to the reduction of the thermalization rate and enhances the hot-electron's relaxation time, which has also been observed in case of other high density materials [85]. Consequently, this feature suggests that electric field confinement helps to excite free electrons to higher energy states, and these non-equilibrium hot-electrons take longer to relax via a series of electron-phonon scattering processes.

3.7 Conclusion

In summary, we have experimentally demonstrated the impact of propagating surface plasmon excitation on the hot-carrier relaxation time through the use of a degenerate pump-probe technique under the Kretschmann configuration. We intro-

duce an approach to analyse the unique internal field confinement in Au thin films with surface plasmon coupling by modifying the two-temperature model. It's worth mentioning that our heat equation does not account for the propagating portion of the surface plasmon, which can in principle deposit optical energy outside of the illuminated area. From the comparison study between the constant absorbed pump power and the constant electric field, we determine that the electric field confinement results in the generation of long-lived hot electrons in the Au thin film. Our results provide a foundation for the design of efficient plasmonic systems to tailor hot-carrier lifetime with low power consumption in hot-carrier based optoelectronic devices.

Chapter 4: Control of hot-carrier relaxation time in Au-Ag thin films through alloying

4.1 Overview

The plasmon resonance of a structure is primarily dictated by its optical properties and geometry, which can be modified to enable hot-carrier photodetectors with superior performance. Recently, metal-alloys have played a prominent role in tuning the resonance of plasmonic structures through chemical composition engineering. However, it has been unclear how alloying modifies the time dynamics of the generated hot-carriers. In this chapter, we elucidate the role of chemical composition on the relaxation time of hot-carriers for the archetypal Au_xAg_{1-x} thin film system. Through time-resolved optical spectroscopy measurements in the visible wavelength range, we measure composition-dependent relaxation times that vary up to 8x for constant pump fluency. Surprisingly, we find that the addition of 2% of Ag into Au films can increase the hot-carrier lifetime by approximately 35% under fixed fluence, as a result of a decrease in optical loss. Further, the relaxation time is found to be inversely proportional to the imaginary part of the permittivity. Our results indicate that alloying is a promising approach to effectively control hot-carrier

relaxation time in metals.

4.2 Introduction

Pure metals, such as gold (Au) and silver (Ag), have long been the most commonly used plasmonic materials due to their high electron densities and desirable optical and chemical properties [16, 86, 87, 88, 89, 90, 91]. However, when using pure metals, applications are limited to a narrow range of optical frequencies stemming from the fixed resonances of the metals. Alloying these metals together presents a promising alternative by allowing the opportunity to tune the plasmonic resonances without altering the geometry of the system. The optical properties of the Au-Ag alloys can be tailored throughout the visible spectrum by modifying the atomic ratio of the two metals [92, 93, 94].

Additionally, by varying the alloy's chemical composition, one can modify the electronic band structure, which results in interband transitions over different incident photon energies. It was recently reported that as the concentration of Au increases in Au-Ag alloyed films, the position of the d-band shifts closer to the Fermi level[95]. This reduces the energy gap for interband transitions, leading to transitions occurring with lower incident photon energies. Similar modification of the threshold of the interband transitions has also been studied in other types of materials such as metal nitrides [96], semiconductors [97], and transition metal dichalcogenides [98]. The resonance tunability and band structure engineering of alloys proves useful in a variety of applications including superabsorbers [99], imaging

probes in biomolecular studies [100], implant devices [101], catalysis [102, 103, 104], photovoltaics [105], and hydrogen sensing [106, 107, 108, 109].

Many of the aforementioned applications rely on significant light absorption within the films or nanostructures. One common approach for absorption enhancement is through coupling the incident photons into surface plasmons, i.e. coherent oscillations of free electrons at the metal-dielectric interface. This process results in the generation of highly energetic non-thermal carriers, also known as hot-carriers. Particularly, hot-carriers are generated after nonradiative decay of the localized or propagating surface plasmons through either direct or phonon-assisted intraband transitions [84, 110]. Once these carriers are excited, they thermalize to create a population of electrons that can be described as a Fermi-Dirac distribution at an elevated temperature. They start to equilibrate with the lattice temperature via a series of scattering processes including the electron-phonon and phonon-phonon scattering[111, 112]. These highly energetic carriers have been utilized in applications such as water splitting [113], artificial photosynthesis [7], medical therapy [114], and drug delivery [115]. However, efficient generation and extraction of these carriers depends on the choice of material, and their corresponding hot-carrier relaxation time. In particular, understanding of the hot-carrier relaxation time plays a significant role in modulation speed [116], power conversion efficiency enhancement [117, 118], determining the hot-electron flux [119, 120], and nanoscale photothermal heat control [121]. Thus, due to the broad spectral tunability associated with devices exploiting hot-carrier physics, their temporal study in planar Au-Ag structures would benefit a variety of applications.

In this chapter, we focus on Au-based hot-carrier devices due to their chemical stability and incorporate different ratios of Ag to create Au-Ag alloys. We use ultrafast pump-probe optical spectroscopy to measure the hot-carrier relaxation time. The pump wavelength is nominally set to 700 nm wavelength (1.77 eV) to ensure that the relaxation time is due to intraband transitions rather than interband ones (2.4 eV in Au and 4.0 eV in Ag) [95, 122]. We employ the Kretschmann geometry to couple into the propagating surface plasmon mode, which has the added benefit of increasing the measurement sensitivity as a result of increased photon absorption. To determine the hot-carrier lifetime, we use a free-electron model and convert the differential reflectivity measurements to the corresponding elevated electron temperature [123]. Our results show that the hot-carrier relaxation time depends upon the Ag mole fractions. We further find that the lifetime is inversely proportional to the imaginary part of the permittivity for different Au-Ag alloys. Finally, considering the pure Au film as the baseline of the lifetime measurements, we observe that the slight addition of Ag (2%) can increase the hot-carrier relaxation time, while higher fractions of Ag (e.g. 35% and 75%) yield smaller lifetimes.

4.3 Fabrication of AuAg alloyed samples

We used a co-sputtering system (AJA International sputtering system) for the alloyed Au-Ag thin film depositions. All sample fabrications, and optical and material testing are performed at the Maryland NanoCenter-FabLab.

Sputtering is a Physical Vapor Deposition (PVD) method in which the energetic

Film composition	Deposition time	Voltage (Au, Ag)	Chamber pressure	Thickness
Au	45 sec	200	4×10^{-6}	35 nm
$Au_{98}Ag_2$	45 sec	(200,100)	3.8×10^{-6}	42 nm
$Au_{65}Ag_{35}$	20 sec	(200,105)	3.7×10^{-6}	25 nm
$Au_{25}Ag_{75}$	15 sec	(100,200)	3.8×10^{-6}	21 nm

Table 4.1: **AuAg alloyed fabrication recipes**

ionized Argon gas generated by applying a high voltage between the cathode (target) and anodes (substrate) accelerates toward the targets. The surface atoms of the targets are then ejected and form a thin film on the substrate surface. The three incorporated targets within this system enable the deposition of the three different materials, metal or dielectric, simultaneously. We only used two of the available targets with gold and silver source pockets.

For each deposition round, the applied vacuum pump runs for ∼3Hours to drop the chamber pressure down to $\sim 4 \times 10^{-6}$ Torr. The glass substrate cleaning procedure for each deposition round is carried out using acetone, IPA, and blow-dry with nitrogen gas. In each deposition, both prism and glass substrate are placed within the same chamber. The glass substrate is then used for further material and optical characterizations. We change the alloy's composition by varying the applied voltage on the Au and Ag targets during each deposition. Table 4.1 summarized the applied voltage, deposition time, initial chamber pressure, and the alloyed samples' final thickness.

4.4 Optical and material characterization of AuAg alloys

The chemical composition of the alloyed samples is determined with energy-dispersive X-ray spectroscopy (EDX) (Fig. 4.1). Figure 4.1b and 4.1c show the AFM

topography and roughness distribution of Au-Ag alloys. Subsequently, we measure the optical properties of our samples with spectroscopic ellipsometry ranging from 200 nm to 1000 nm (See appendix A for the ellipsometry data and their fits).

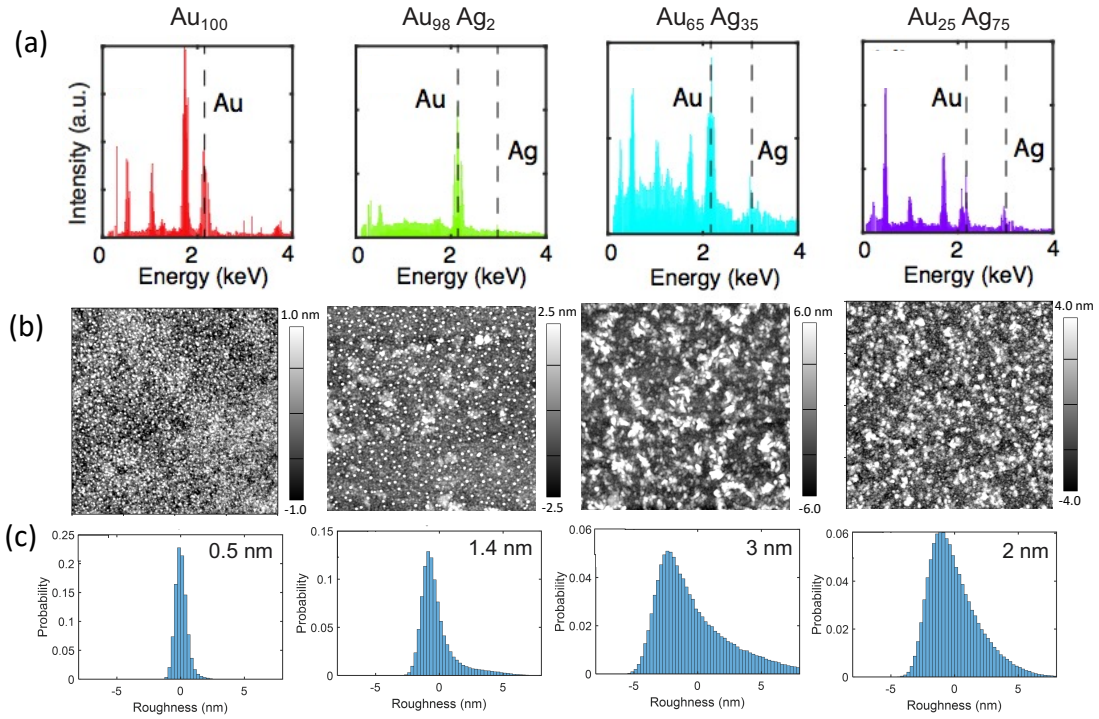

Figure 4.1: Chemical and structural properties of thin films. (a) EDX. (b) AFM topography. (c) Roughness distribution. Insets show RMS roughnesses.

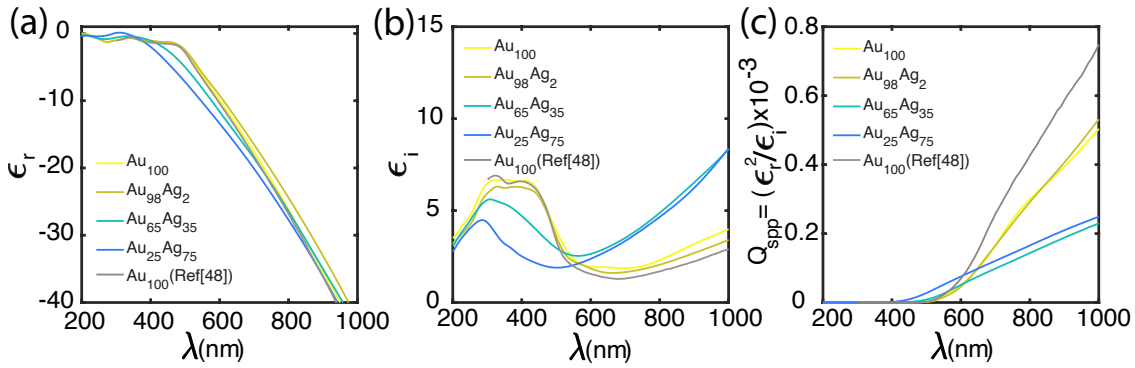

Figure 4.2: Measured (a) real and (b) imaginary parts of the permittivity, and (c) computed quality factor of the propagating surface plasmon of Au_xAg_{1-x} alloys.

We use a Drude-Lorentz model including two Drude and one Lorentz terms to

fit the ellipsometry data. The modelled permittivity is shown in Fig. 4.2a and 4.2b for our fabricated samples. We also compute the surface plasmon polariton (SPP) quality factor, $Q_{spp}\ (\omega) = \epsilon_r^2(\omega)/\epsilon_i(\omega)$ [124], for the different Au-Ag alloys (Fig. 4.2c). In general, many experimental factors such as the chamber pressure, substrate temperature, deposition rate, etc. can affect the films' quality factors due to the change in the dielectric functions [125]. Our experiments keep all of these other factors the same, thus isolating the effects of changing the alloy composition. At 700 nm, the wavelength used for our pump-probe measurements, the 100% Au and 98% Au samples show a higher Q_{spp} when compared to the other alloys, predominantly due to the lower ϵ_i. The dielectric functions can also be affected by a disordered mixture of Au and Ag at a certain molar combination, leading to the reduction of electron scattering and plasma frequency [95, 126]. Additionally, it has been shown that the co-sputtering of a small amount of metal suppresses the island growth, leading to a film with low optical and electrical losses [105]. Furthermore, the imaginary part of the dielectric function of a thin film, which is responsible for the optical losses, generally increases with the decrease of the film thickness for gold films below 80 nm [127]. We have compared the optical properties of our pure gold sample with that of a pure gold film obtained from [127] (gray lines in Fig. 4.2), showing good agreement. We further hypothesis that by varying the thickness of the different AuAg alloys, the relaxation time of the excited hot-carriers could be further tuned due to the variation in the optical losses in these films.

4.5 Surface plasmon coupling in the alloyed samples

Before measuring the relaxation dynamics of the excited hot-carriers, we measured the propagating surface plasmon mode using the Kretschmann configuration [128]. Figure 4.3b shows the experimental results of the reflection measurements for all four samples as a function of incident angle near the plasmon coupling angle for incident wavelength from 680 nm to 740 nm with 5 nm spectral bandwidth.

We utilized the Finite Difference Time Domain (FDTD) method (Lumerical Inc.) for the reflection calculations (Fig. 4.3b). The optical properties of the samples are extracted from the ellipsometry measurements and used as inputs for the simulations. A perfectly match layer (PML) boundary condition with 64 layers is used for the boundaries along with a non-uniform mesh setting with an accuracy of 4. The source is a plane wave and the incident angle is swept from 40 to 48 degrees with 0.1-degree increments for each wavelength between 680 nm and 740 nm. There is a good agreement between the FDTD simulation results and the experimental measurements. As expected, the surface plasmon resonance is sharper for samples with higher Q_{spp} and broader for the samples with lower values.

4.6 AuAg alloys and time-resolved differential reflectively measurements

Similar to the previous chapter, the non-equilibrium hot-carrier dynamics of the alloys are investigated using degenerate ($\lambda_{pump} = \lambda_{probe}$) time-resolved differ-

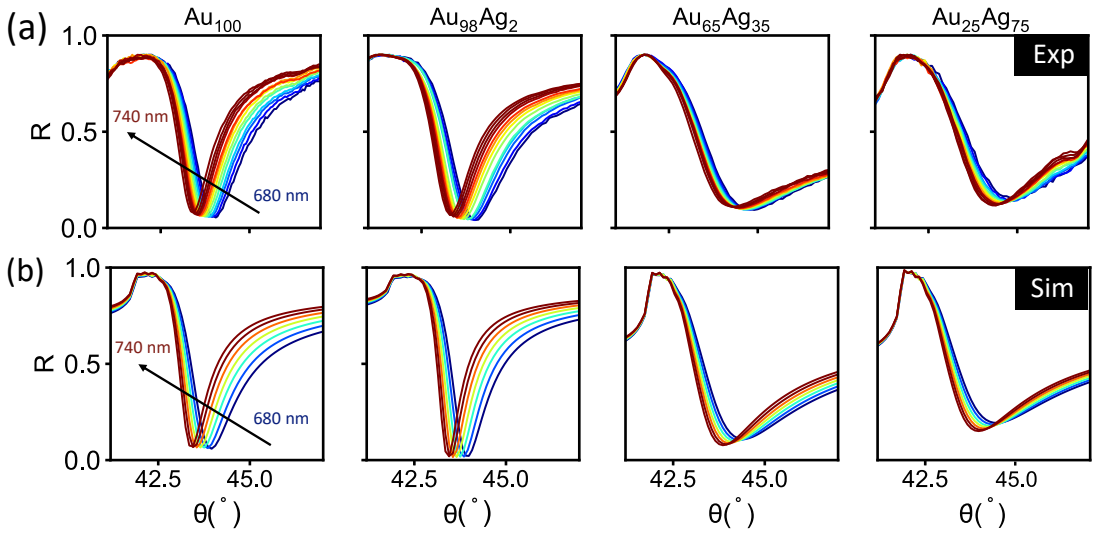

Figure 4.3: (a) Experimental and (b) simulated reflectivity for Au, $Au_{98}Ag_2$, $Au_{65}Ag_{35}$, and $Au_{25}Ag_{75}$ alloys under p-polarized illumination with wavelengths ranging from 680 nm to 740 nm. For FDTD simulations, we used pulse illumination with 150 fs pulse width.

ential reflectivity measurements at the surface plasmon resonance angle. We use a Ti-Sapphire laser system with 700 nm wavelength and 80 MHz repetition rate to generate both the pump and probe beams. A fraction of the laser beam is split off to serve as the probe beam and the other portion is passed through a mechanical delay stage to set the time delay between the two beams. We use nearly co-linear pump and probe beams, which are adjusted to couple into the propagating surface plasmon mode but can also be spatially separated in the reflected field. The overlap of the beams is achieved using an off-axis parabolic mirror with a measured spot size of approximately 90 μm. Pump-probe measurements are conducted at the surface plasmon resonance angle under five different incident pump powers (i.e. 120 mW, 150 mW, 180 mW, 210 mW, and 240 mW) with a fixed probe power of 19.8 mW, as shown in Fig.4.4.

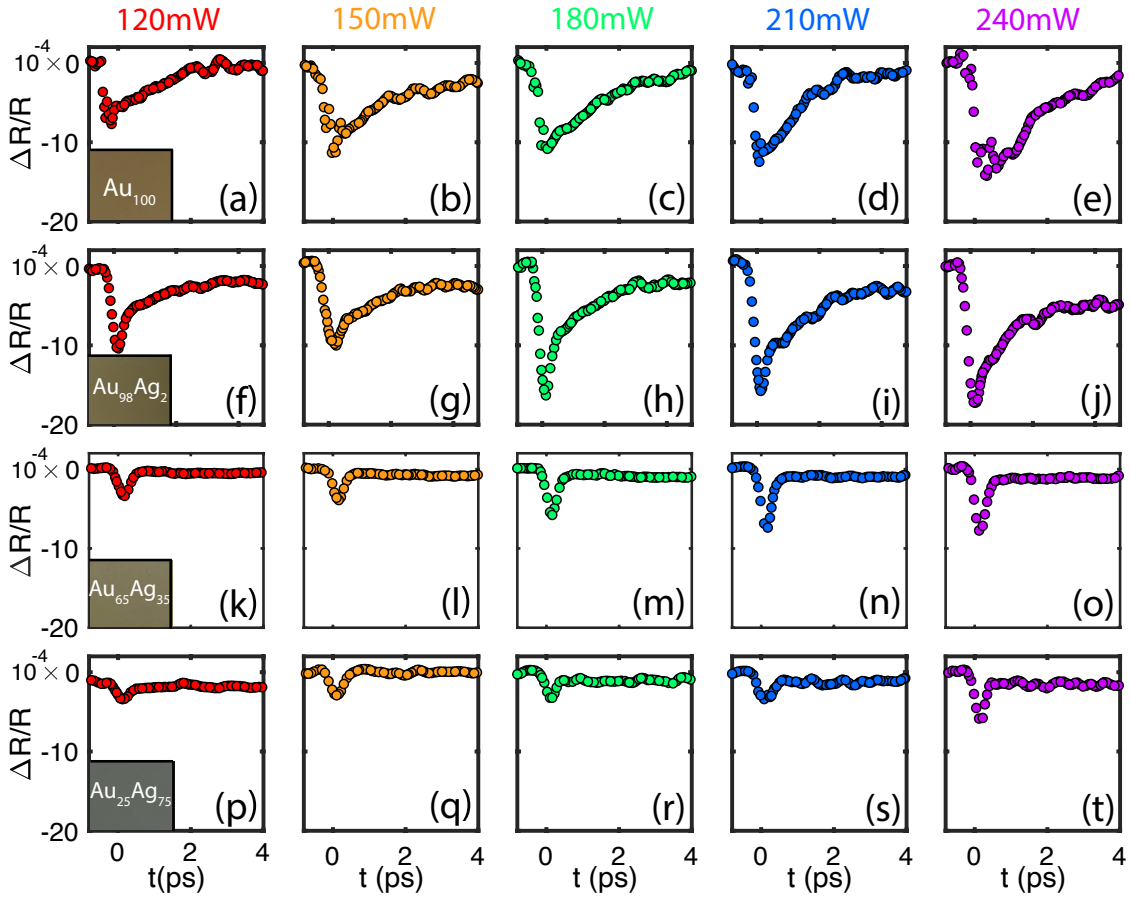

Figure 4.4: Differential reflectivity measurements for Au-Ag alloys with different chemical compositions. For each sample, the pump power is: 120 mW (a,f,k,p), 150 mW (b,g,l,q), 180 mW (c,h,m,r), 210 mW (d,i,n,s), and 240 mW (e,j,o,t). Insets are real-color photographs of the alloyed thin films.

As expected, in all cases, increasing the pump power produces a larger change in the transient reflectivity ($\Delta R/R$). Because the temporal pulse width employed here is longer than the electron-electron scattering time, on the order of 100 fs [129], the relaxation time for the optically excited hot-carriers is mostly governed by the electron-phonon relaxation time.

It is also worth mentioning that both hot-electrons and hot-holes can contribute to device performance, see for example the use of hot-holes for photochemical reactions [130]. Gong *et al.* showed how the energy of the hot-carrier distribution

depends not only on the Electron Density of States (EDS) but also on the energy of the incident photons and how it can be modified for a variety of structures [131]. For the 700 nm wavelength illumination used in our study, hot-hole extraction is more efficient than the hot-electrons extraction in pure Au, as the distribution of hot-holes is peaked further away from the Fermi level. However, for the case of the Au-Ag mixtures, the distributions of both hot-holes and hot-electrons become more uniform as the illumination wavelength approaches the Near-IR range [132]; thus, both of these excited hot-carriers will have similar contributions to the overall hot-carrier effects. We also note that the differences between the hot-hole and hot-electron distributions in Au and Au-Ag alloys can provide additional tunability for the carrier extraction depending upon the materials and functionality of the rest of the device. Further, the threshold for the interband transition for Au-Ag alloys shifts to a longer wavelengths as the Au content increases, allowing for additional control of these processes [95, 132].

4.7 Data analysis

To find the excited hot-carrier relaxation time from the transient reflectivity measurements, we employ the combination of a free-electron model [133] and the modified two-temperature model [123]. In this model, the effect of the surface plasmon's electric field profile is incorporated into the absorbed laser power density within the conventional two-temperature model, which accounts for variation of the field in the vertical (surface normal) direction. This combination allows us to convert

the pump-probe reflectivity signal to the relevant electron temperature, which results in more accurate theoretical modeling due to the nonlinear relationship between the reflectivity signal and the electron temperature. The model uses the optical parameters extracted from our ellipsometry measurements at room temperature for each alloy. Finally, best fits to the temperature converted reflectivity signals are computed by minimizing the Normalized Mean Squared Error (NMSE) of the hot-carrier relaxation time. Figure 4.5 shows the results of the temperature converted data (filled circles) and their corresponding best fits (solid lines) to the hot-carrier relaxation time of the alloyed Au-Ag films at pump powers of 120 mW, 150 mW, 180 mW, 210 mW, and 240 mW under the resonance condition, i.e. upon coupling to the surface plasmon mode.

The pump-probe measurements also reveal an additional short decay component that only appears immediately after excitation for the 2% Ag composition. We attribute this decay component to electron-electron interactions, which are typically too fast to be detected in the pure Au. The plasmon dephasing time (i.e. the rate at which electron's collective oscillations cease) is longer in Ag as a result of different radiative or non-radiative plasmon damping mechanisms, and so the addition of Ag to the Au alloy may increase this decay component to a measurable amount in the 2% Ag alloy. For the higher Ag concentration alloys, this decay mechanism is not distinguishable from electron-phonon interactions based on our measurement sensitivity.

Analysis of the temperature converted differential reflectivity shows that the hot-carrier relaxation time (τ) of the $Au_{98}Ag_2$ sample is 8$\times$ larger than for $Au_{65}Ag_{35}$

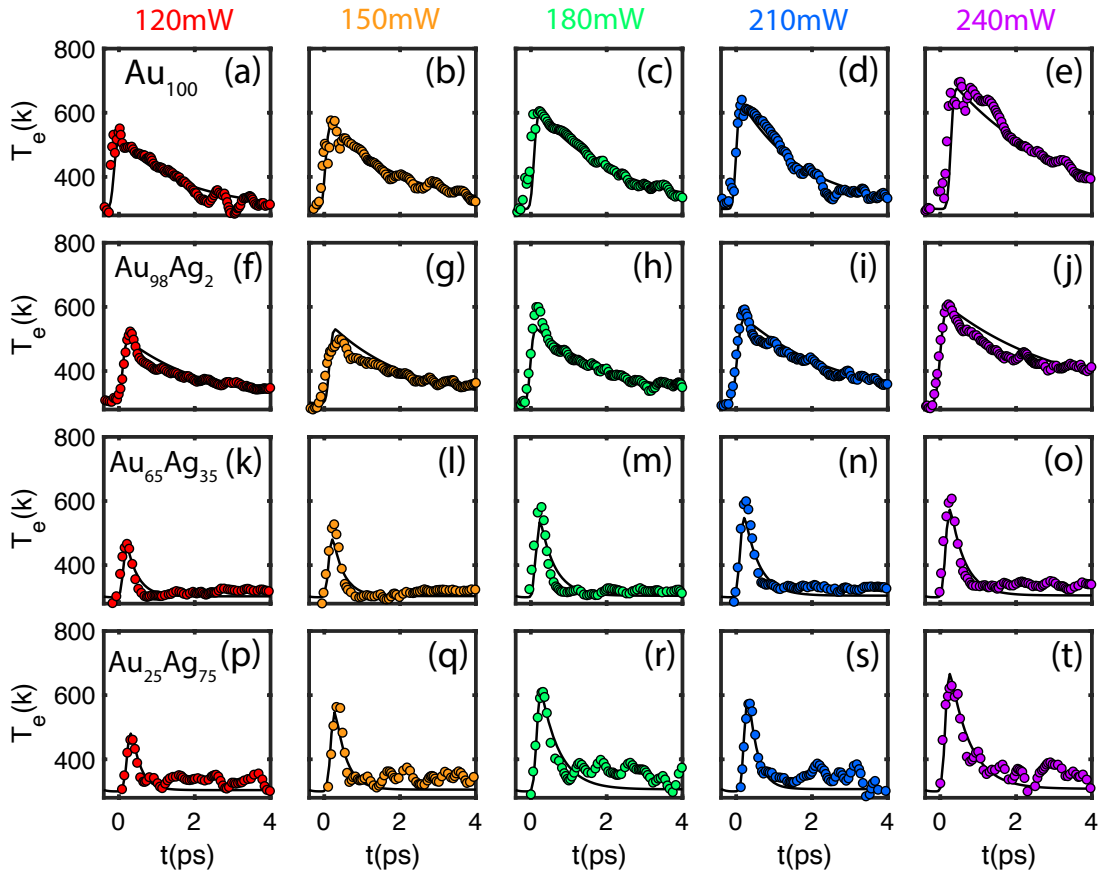

Figure 4.5: Temperature converted differential reflectivity measurements for Au_{100}, $Au_{98}Ag_2$, $Au_{65}Ag_{35}$, and $Au_{25}Ag_{75}$ alloys under different incident pump powers of 120 mW (a,f,k,p), 150 mW (b,g,l,q), 180 mW (c,h,m,r), 210 mW (d,i,n,s), and 240 mW (e,j,o,t). The black solid lines in each plot show the best fits computed from a modified two-temperature model.

and $Au_{25}Ag_{75}$ for a fixed laser fluence. Additionally, we find that the film with $Au_{98}Ag_2$ has the longest lifetime of any of the samples measured (3.20 $\pm$ 0.15 ps with 240 mW pump power), even including pure Au. To further investigate this phenomenon, we consider the optical properties of each Au-Ag alloy at 700 nm pump wavelength and compare the result with our measured hot-carrier relaxation time, and find τ to be inversely proportional to the imaginary part of the permittivity (See Fig. 4.6).

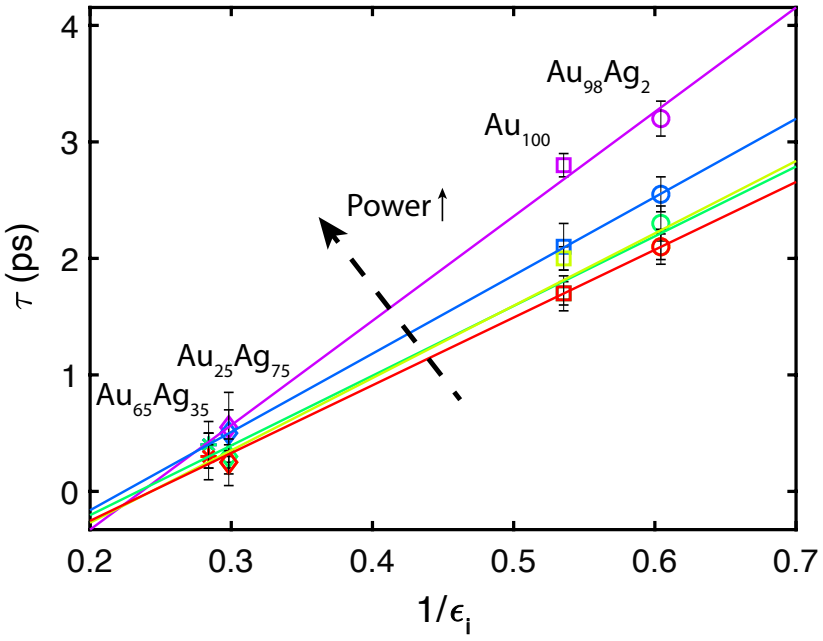

Figure 4.6: Hot-carrier relaxation time as a function of $1/\epsilon_i$, the inverse of the imaginary part of the permittivity, for Au_xAg_{1-x}. The solid lines are the linear fit between the hot-carrier lifetime and $1/\epsilon_i$. The colors represent the range of the pump power between 120 mW (red) to 240 mW (purple).

Our results suggest that the addition of a small fraction (2%) of Ag to a Au film increases the hot-carrier lifetime. This is consistent with previous findings that showed particular Ag-Au alloys having higher Q_{spp} than pure metals [94] and that doping one metal with another can improve film quality and decrease optical loss [105, 134]. However, all alloyed films that we measured have similar surface roughnesses, suggesting that the decreased loss may come from changes in the band structure or other changes to the material rather than simply smoothing of the films. Because we are probing relaxation times >10s of fs, the main mechanism leading to the increase in the hot-carrier lifetime is likely a suppression of the electron-phonon scattering, which could result for decreased lattice defects, grain boundaries,

etc., but further work will be necessary to isolate the individual contributions. In addition, the lifetime is inversely proportional to ϵ_i and increases with pump power (see Fig. 4.6 for a comparison with all pump powers), which is in agreement with previously reported studies [135, 136]. However, this is an empirical observation, and not a strict mathematical proportionality that is grounded in theory. Our measurements show that the optical loss is an important and potentially controllable internal parameter compared to the other external factors, such as pump power. Our observation further opens a new route to alter the hot-carrier relaxation time for plasmonic applications through alloying.

4.8 Conclusion

In summary, we measured the hot-carrier relaxation time of Au-Ag thin film alloys under visible excitation and found that adding a small fraction of Ag to Au increases the hot-carrier relaxation time. Our experimental results suggested that the relaxation time depends on the alloy's composition and is inversely proportional to ϵ_i. Surprisingly, some alloys can have loss factors that are less than their pure counterparts, which leads to improved hot-carrier performance. By comparing the relaxation time of the fabricated alloys with the pure Au sample, we determined that the measured relaxation time increases with slight addition of Ag and then drops significantly for alloys with higher Ag content. Overall, this work demonstrated that the relaxation time of hot-carriers can be engineered through alloying.

Chapter 5: Hot-carrier temporal dynamics in AuCu alloy

5.1 Sample fabrication and optical measurements

To probe the alloying effect on the hot-electrons' temporal dynamics, we further fabricate AuCu alloys with different compositions. The same fabrication process as in the case of AuAg (Chapter 4) is also performed here. EDX and ellipsometry measurements are used to determine the material compositions and dielectric functions of the AuCu alloys (Fig. 5.1). The samples' thicknesses are determined by fitting the B-spline model on the ellipsometry data, resulting in 43 nm, 47 nm, and 49 nm for samples from high to low Au concentration (i.e. $Au_{70}Cu_{30}$, $Au_{57}Cu_{43}$, and $Au_{54}Cu_{46}$), respectively. Figure (5.2) shows the results of the surface plasmon coupling experiment and simulation on these alloys repeated for wavelengths ranging from 680 nm to 740 nm. Considering approximately the same thickness for these alloys, the surface plasmon coupling reduces as the copper composition increases. Among these samples, the only detectable pump-probe signal is for the $Au_{70}Cu_{30}$ sample with $\sim$70% absorption at resonance.

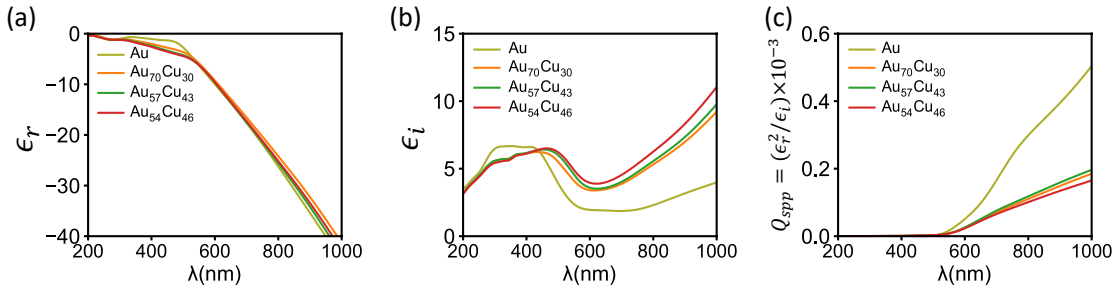

Figure 5.1: The (a) real, (b) imaginary part of the dielectric function of Au_xCu_{1-x} alloys, and (c) their corresponding surface plasmon quality factor (Q_{spp}) with x = 100, 70, 57, and 54. The results are determined from fits to the spectroscopic ellipsometry data. The composition of each sample is measured by energy-dispersive X-ray spectroscopy (EDX).

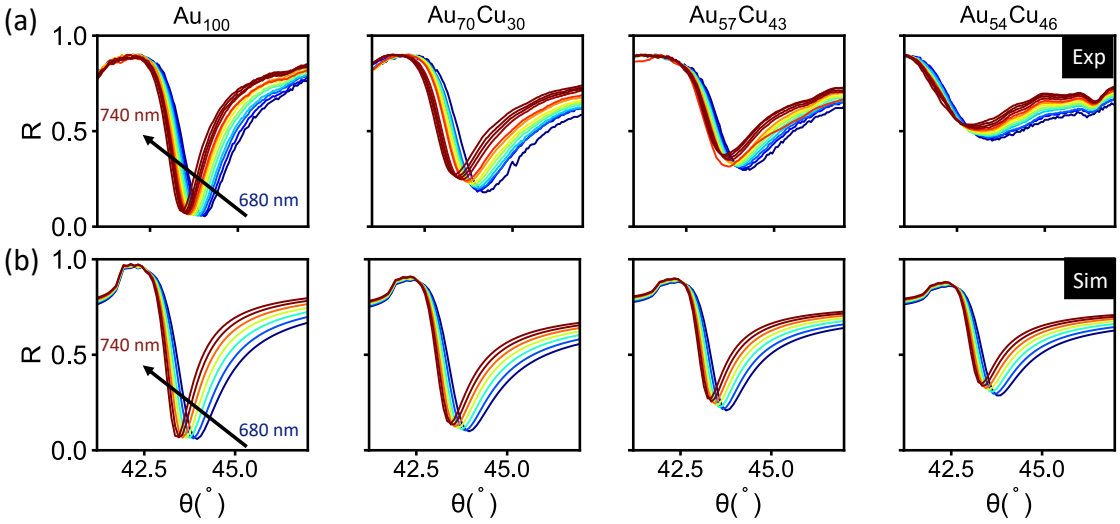

Figure 5.2: (Top row) Experimental and (bottom row) numerical simulation of surface plasmon polariton excitation of Au_xCu_{1-x} alloys with x = 100, 70, 57, and 54. The wavelength range is from 680 nm to 740 nm.

5.2 Hot-carrier temporal dynamics in AuCu alloys

Figure (5.3) illustrates the recorded transient response of the $Au_{70}Cu_{30}$ alloys with pump power ranging from 210 mW to 300 mW and a fixed probe power of 17 mW. These measurements are performed at resonance and under a wavelength of 700 nm for both pump and probe beams.

A coherent interference artifact appears near zero-time delay, especially for the case of lower pump power when the signal is small. This effect happens due to the spatial overlapping of the two pump and probe beams. The two-beam interference generates a spatial modulation of the refractive index on the sample surface results the diffraction of the pump pulse into the direction of the probe beam[137]. The diffracted pump has an opposite phase compared to the probe and leads to a decrease in the probe beam's amplitude. Thus, the recorded pump-probe signal can be affected by the interference patterns for the case of the degenerate pump-probe measurements. Interference artifacts are more detectable in the AuCu alloys under lower fluences. As the absorbed pump power increases, the signal gets enhanced and overcomes these artifacts.

In these alloys, the random atomic structure destroy the periodicity of the crystal structure [122]. This effect results in the higher imaginary part of the dielectric response above 500 nm (Fig. 5.1). Using the Drude model, the imaginary part of the dielectric function is proportional to the Drude damping factor, which itself is inversely proportional to the electron mean free path. Thus, we can conclude that the higher loss in these samples results in the lower electron mean free path, and consequently higher scattering phenomena, and a reduction of the hot-electron relaxation time.

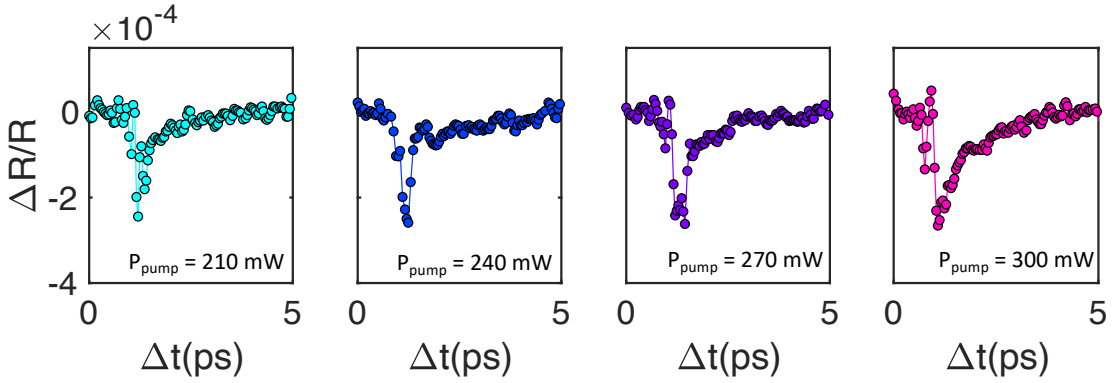

Figure 5.3: Transient differential reflectivity measurements of $Au_{70}Cu_{30}$ alloy at different pump powers (210 mW to 300 mW) while coupling to the propagating surface plasmon. Pump and probe wavelengths are 700 nm.

5.3 Conclusion

Just as we observed in the previous two chapters, faster hot-carrier relaxation times occur under low pump power. Here, the relaxation time under the maximum pump fluence for the $Au_{70}Cu_{30}$ sample reaches 0.9 ps which is almost half of what we measured in the $Au_{98}Ag_2$ alloy. This result could be due to the lower absorption ($\sim$70%) compared to the $Au_{98}Ag_2$ sample. However, for a better comparison, measurements of the hot-electron relaxation time are needed over a larger compositional range.

Chapter 6: Conclusion and future directions

6.1 Hot-carrier temporal dynamics in non-metallic materials

This dissertation specifically investigated the temporal dynamics of the hot-electrons in metal films and metallic alloys. The reason is, in fact, much of the current experimental work on nanophotonic and plasmonic systems have either utilize gold or silver due to their simple fabrication process and relatively low losses in the visible and NIR frequencies. However, in some plasmonic systems, such losses are still detrimental to the overall performance of the devices. Furthermore, Au and Ag are not compatible with the CMOS technologies used for the integrated circuits industry [138]. Another point that could make gold less desirable for hot-carrier collection is its high work function. As a result, there is a large barrier height between the gold-semiconductor junction. Therefore, it makes the collection of hot-electrons generated with lower energy photons more challenging. Thus, alternative plasmonic materials such as intermetallics (a mixture of metals with non-metallics such as nitrides), ceramics, and semiconductor-based materials have emerged to overcome these limitations. For instance, titanium nitride (TiN) is a ceramic material that is considered as an alternative to the conventional plasmonic metals such as gold in the visible and near-infrared frequencies because of the similarity of its optical

properties to those in gold beyond 500 nm[139]. It also overcomes drawbacks of conventional plasmonic metals' based on its lower cost, higher melting point, and chemical stability. Additionally, it is appealing for manufactured electronics devices due to its compatibility with the CMOS technology. Further, its broad range tunability using different fabrication techniques adds to its advantages. Thus, studying hot-carrier temporal dynamics in non-metallic materials with possibly lower loss would be another interesting direction.

6.2 Hot-carrier temporal dynamics in TiN sample

Besides low loss (around 500 nm) and similar optical properties to gold, another advantage of TiN sample (Fig. 6.1) is that it supports an ENZ (Epsilon-near-zero) property in the visible range.

ENZ materials exhibit a near-zero real part of the dielectric function at a wavelength known as the zero-permittivity wavelength [140] with major applications in optical switching devices. Also, not all materials with ENZ properties can support an ENZ mode. Such a mode can be excited when the film's thickness is sufficiently thin [141]; thus, enabling a high photon absorption and electromagnetic field confinement at the resonance. Recent studies have measured the a hot-electron relaxation time of $\sim$ 350 ps for TiN samples [142], which is without considering any ENZ mode. The ENZ mode excitation in such materials is another promising direction for modifying the hot-electron time dynamics.

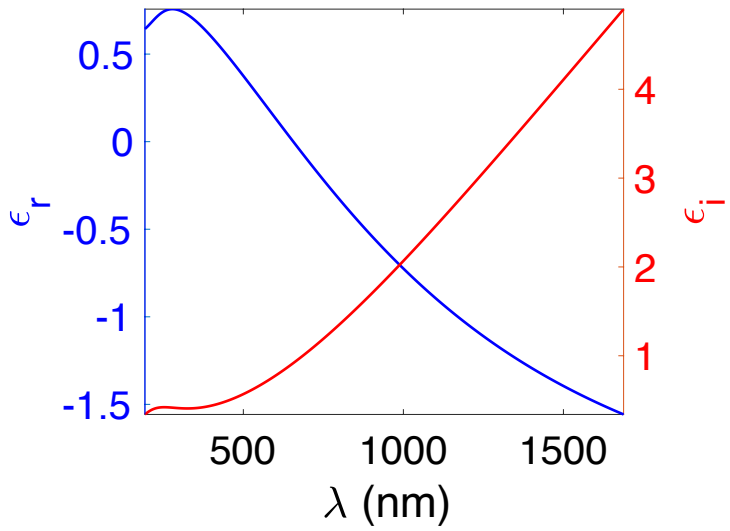

Figure 6.1: Real (red) and imaginary (blue) parts of the measured dielectric function of 22 nm TiN fabricated by pulsed laser deposition. The permittivity data is obtained from the ellipsometry fit (see figure A.5).

6.3 X-ray diffraction microscopy on AuAg samples

The hot-electron relaxation enhancement observed for the $Au_{98}Ag_2$ film is something that requires additional material analysis. To understand the origin of such enhancement, the next step could be to perform X-ray diffraction measurements (XRD). This would help us to determine the crystalline features of the film; as the reduced grain sizes can result in a reduction of the electron scattering. Also, it's important to understand the material properties of the prism itself. The prism used for these measurements is an N-BK7 right-angle prism with an anti-reflection coating on the hypotenuse. However, the ellipsometry measurements are performed on the glass slide which is mounted in the same deposition chamber as the prism. The surface of the prism will also affect the metal film and should be further analyzed in future experiments.

6.4 Conclusion

In this dissertation, we measured the relaxation time of the excited hot-electrons in metal films and metallic alloys by employing a degenerate pump-probe spectroscopy setup. With the advantage of coupling to the propagating surface plasmon, we were able to increase the absorption and further tune the hot-electron relaxation dynamics within metallic films and alloys. Results from hot-carrier temporal measurements on different alloys (AuAg and AuCu) show that the relaxation time heavily depends on the material compositions and can be controlled by selecting a proper ratio. Finally, We anticipate that this study could lead to the efficient design of future hot-electron-based devices.

Appendix A:

A.1 Fabrication procedure

All sample fabrications are performed at the Maryland NanoCenter-FabLab. Angstrom e-beam evaporator is utilized, which is configured for the metal depositions. In this system, electron beams are emitted off of the tungsten filament at a very high temperature. Both prism and glass substrate are loaded within the same chamber. For each deposition round, the applied vacuum pump runs for 3 hours to drop the chamber pressure down to $\sim 4 \times 10^{-6}$ Torr. The glass substrate cleaning procedure for each deposition round is carried out using acetone, IPA, and blow-dry with nitrogen gas.

A.2 Ellipsometry data of AuAg alloys

Spectroscopic ellipsometry data measured for the alloy samples are depicted in Fig.A.1. Peak shift in the transmission spectrum (Fig.A.2 of the alloyed sample deposited on glass substrate from pure gold at ∼520 nm to $Au_{25}Ag_{75}$ at ∼400 nm) shows a progressive decrease in the inter-band transition due to lower gold concentrations. These results agree with the Gong et al. [94] study of transmission

spectra of noble metal alloyed thin films.

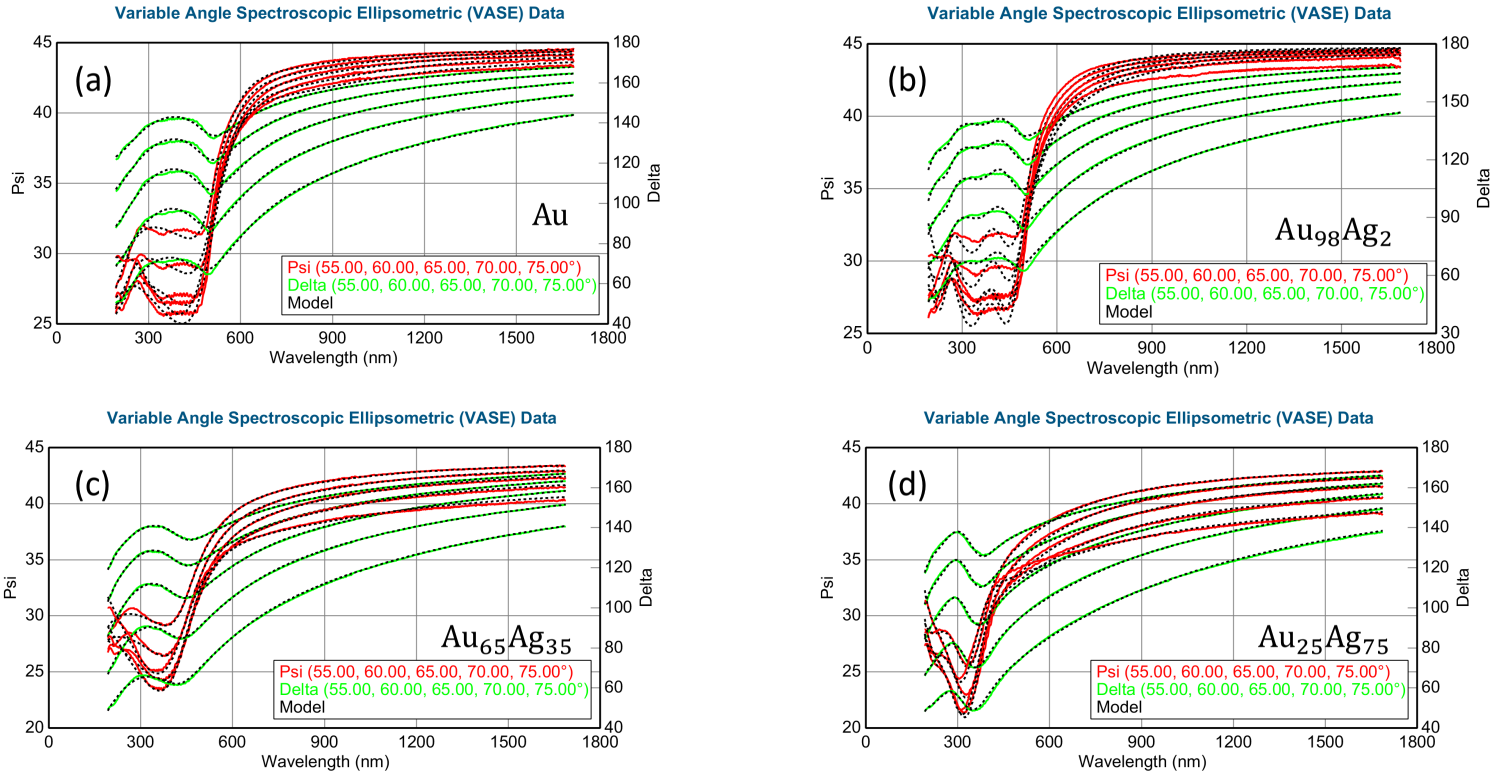

Figure A.1: Ellipsometry data: Delta (green line) and Psi (red line) for four different alloy mixtures, (a) Au, (b) $Au_{98}Ag_2$, (c) $Au_{65}Ag_2$, and (d) $Au_{25}Ag_{75}$ at five different incident angles with their corresponding best fits (dashed lines). We use the GenOsc model to fit the data. Both optical properties and thickness are obtained from the fits.

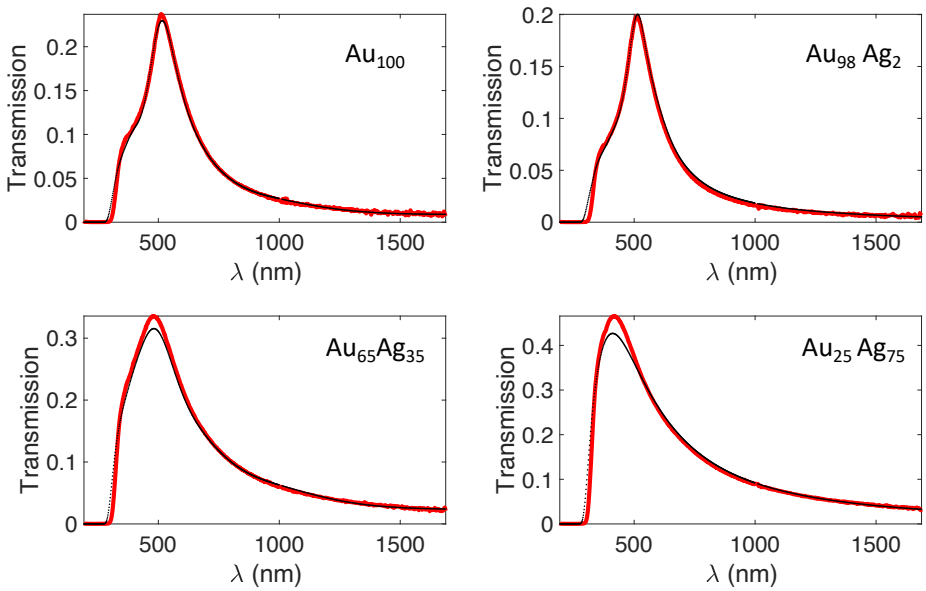

Figure A.2: Transmission spectra obtained from the spectroscopic ellipsometry measurements on AuAg alloyed film on glass. The solid red lines show the ellipsometry data and the dotted black lines indicate the fit on data using a B-spline model.

Film composition	EDS (%)	Deposition time	Voltage (Au, Cu)	Chamber pressure	Thickness
AuCu	70,30	45 sec	(200,100)	4.2×10^{-6}	43 nm
AuCu	57,43	45 sec	(200,150)	4.4×10^{-6}	47 nm
AuCu	54,46	45 sec	(100,180)	4.9×10^{-6}	49 nm

Table A.1: **AuCu alloyed fabrication recipes**

A.3 Ellipsometry data of AuCu alloys

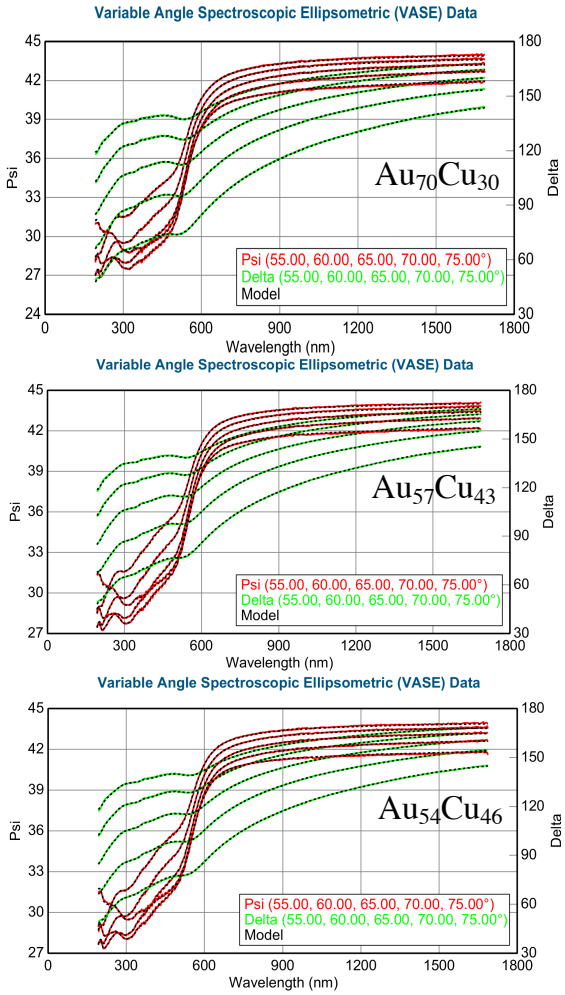

Figure A.3: Ellipsometry data and fit on the AuCu alloys.

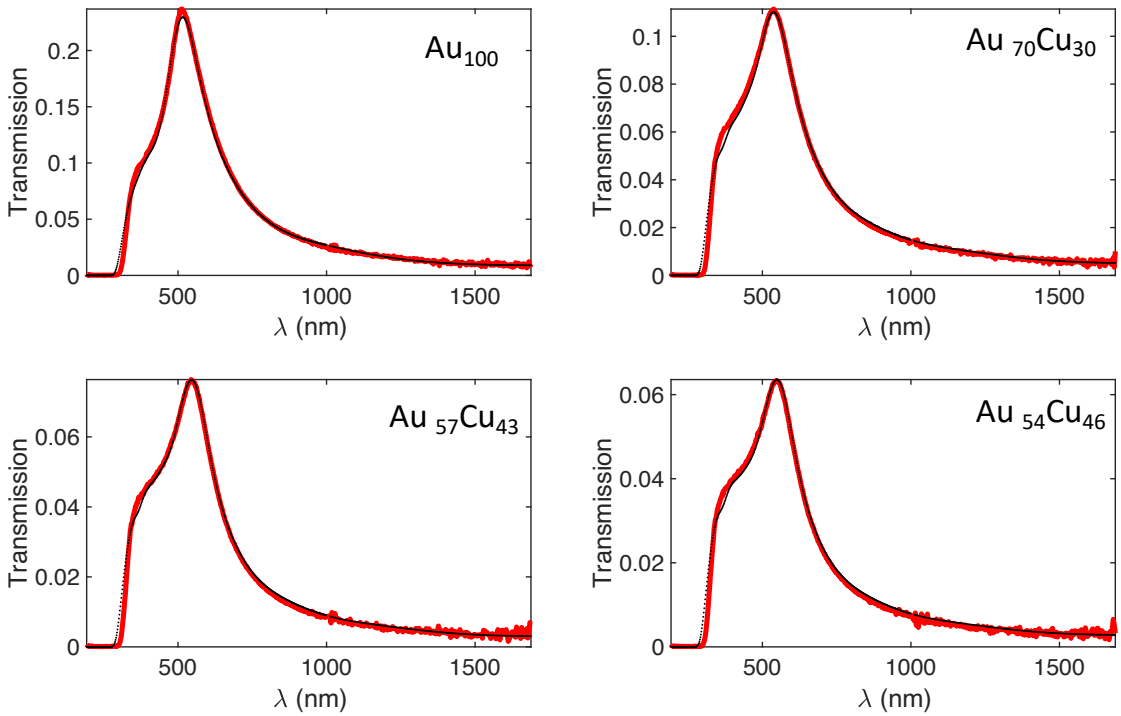

Figure A.4: Transmission spectra obtained from the spectroscopic ellipsometry measurements on AuCu alloyed film on a glass. Transimission peak shift from 550 nm for the pure Au to about 600 nm for the sample with higher Cu percentage.

A.4 Ellipsometry data of TiN

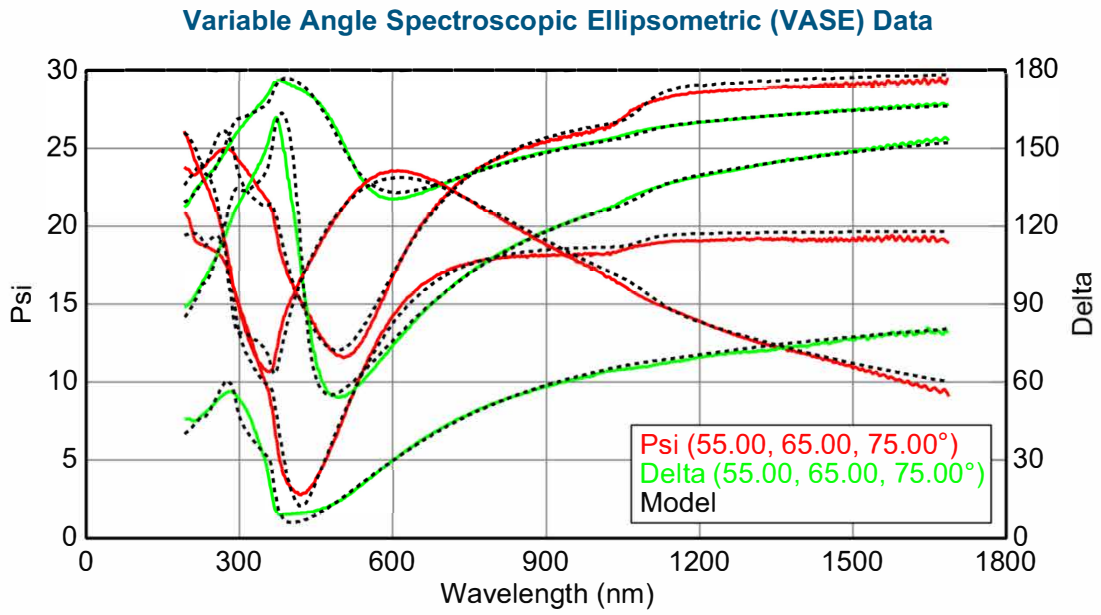

Figure A.5: Ellipsometry data (solid lines) and a model fit (dashed lines) on a 22 nm TiN film on Si substrate fabricated by pulsed laser deposition.

Bibliography

[1] Mark W Knight. Photodetection with Active. *Science*, 702(2011):702–704, 2011.

[2] Ali Sobhani, Mark W Knight, Yumin Wang, Bob Zheng, Nicholas S King, Lisa V Brown, Zheyu Fang, Peter Nordlander, and Naomi J Halas. Narrowband photodetection in the near-infrared with a plasmon-induced hot electron device. *Nature Communications*, 4:1–6, 2013.

[3] Boris S. Karasik, Andrei V. Sergeev, and Daniel E. Prober. Nanobolometers for THz photon detection. *IEEE Transactions on Terahertz Science and Technology*, 1(1):97–111, 2011.

[4] A. Shurakov, Y. Lobanov, and G. Goltsman. Superconducting hot-electron bolometer: From the discovery of hot-electron phenomena to practical applications. *Superconductor Science and Technology*, 29(2), 2015.

[5] Xinghan Cai, Andrei B. Sushkov, Ryan J. Suess, Mohammad M. Jadidi, Gregory S. Jenkins, Luke O. Nyakiti, Rachael L. Myers-Ward, Shanshan Li, Jun Yan, D. Kurt Gaskill, Thomas E. Murphy, H. Dennis Drew, and Michael S. Fuhrer. Sensitive room-temperature terahertz detection via the photothermoelectric effect in graphene. *Nature Nanotechnology*, 9(10):814–819, 2014.

[6] Xinghan Cai, Andrei B. Sushkov, Mohammad M. Jadidi, Luke O. Nyakiti, Rachael L. Myers-Ward, D. Kurt Gaskill, Thomas E. Murphy, Michael S. Fuhrer, and H. Dennis Drew. Plasmon-Enhanced Terahertz Photodetection in Graphene. *Nano Letters*, 15(7):4295–4302, 2015.

[7] Syed Mubeen, Joun Lee, Nirala Singh, Stephan Krämer, Galen D. Stucky, and Martin Moskovits. An autonomous photosynthetic device in which all charge carriers derive from surface plasmons. *Nature Nanotechnology*, 8(4):247–251, 2013.

[8] Alberto Naldoni, Urcan Guler, Zhuoxian Wang, Marcello Marelli, Francesco Malara, Xiangeng Meng, Lucas V. Besteiro, Alexander O. Govorov, Alexander V. Kildishev, Alexandra Boltasseva, and Vladimir M. Shalaev. Broadband

Hot-Electron Collection for Solar Water Splitting with Plasmonic Titanium Nitride. *Advanced Optical Materials*, 5(15):1–11, 2017.

[9] Luca Mascaretti, Aveek Dutta, Štěpán Kment, Vladimir M Shalaev, Alexandra Boltasseva, Radek Zbořil, Alberto Naldoni, L Mascaretti, Š Kment, R Zbořil, A Naldoni, A Dutta, V M Shalaev, and A Boltasseva. Plasmon-Enhanced Photoelectrochemical Water Splitting for Efficient Renewable Energy Storage. *Advanced Optical Materials*, 1805513:1–23, 2019.

[10] Gavin Conibeer. Third-generation photovoltaics. *Materials Today*, 10(11): 42–50, 2007.

[11] Alain Dereux & Thomas W. Ebbesen William L. Barnes. Surface plasmon subwavelength optics. *Nature*, 424:824–830, 2003.

[12] Jiří Homola. Surface Plasmon Resonance Sensors for Detection of Chemical and Biological Species. *Chem. Rev*, 108:462–493, 2008.

[13] Maung Nyan Win, Joshua S. Klein, and Christina D. Smolke. Codeine-binding RNA aptamers and rapid determination of their binding constants using a direct coupling surface plasmon resonance assay. *Nucleic Acids Research*, 34 (19):5670–5682, 2006.

[14] Satoshi Kawata, Yasushi Inouye, and Prabhat Verma. Plasmonics for near-field nano-imaging and superlensing. *Nature Photonics*, 3(7):388–394, 2009.

[15] Christy L. Haynes, Adam D. McFarland, and Richard P. Van Duyne. Surface-enhanced: Raman spectroscopy. *Analytical Chemistry*, 77(17):339–346, 2005.

[16] Stefan A. Maier. *Plasmonics: Fundamentals and Applications*. Springer, 2018. ISBN 5856420187.

[17] L William and W Thomas. Surface plasmon subwavelength optics. *Nature*, 424(14), 2003.

[18] Lukas Novotny and Bert Hecht. *Principles of Nano-Optics*, page 378–418. Cambridge University Press, 2006.

[19] Vincenzo Amendola, Roberto Pilot, Marco Frasconi, Onofrio M. Maragò, and Maria Antonia Iatì. Surface plasmon resonance in gold nanoparticles: A review. *Journal of Physics Condensed Matter*, 29(20):1–48, 2017.

[20] William L. Barnes. Surface plasmon-polariton length scales: A route to sub-wavelength optics. *Journal of Optics A: Pure and Applied Optics*, 8(4):S87–S93, 2006.

[21] R W Wood. On a Remarkable Case of Uneven Distribution of Light in a Diffraction Grating Spectrum. *Proc. Phys. Soc. London*, 18:269–275, 1902.

[22] Andreas Otto. Excitation of Nonradiative Surface Plasma Waves in Silver by the Method of Frustrated Total Reflection. *Zeitschrift ffir Physik*, 216: 398–410, 1968.

[23] E Kretschmann and H Raether. Radiative Decay of Non Radiative Surface Plasmons Excited by Light. *Naturforsch*, 23:2135–2136, 1968.

[24] Alireza Shahsafi, Yuzhe Xiao, Jad Salman, Bradley S Gundlach, Chenghao Wan, Patrick J Roney, and Mikhail A Kats. Mid-infrared Optics Using Dielectrics with Refractive Indices Below Unity. *Physical Review Applied*, 10: 34019, 2018.

[25] Alireza Shahsafi, Jad Salman, Bryan E Rubio Perez, Yuzhe Xiao, Chenghao Wan, and Mikhail A Kats. Infrared Polarizer Based on Direct Coupling to Surface Plasmon Polaritons. *Nano Letters*, 20:8483–8486, 2020.

[26] C. Ropers, C. C. Neacsu, T. Elsaesser, M. Albrechty, M. B. Raschke, and C. Lienau. Grating-coupling of surface plasmons onto metallic tips: A nanoconfined light source. *Nano Letters*, 7(9):2784–2788, sep 2007.

[27] Anatoly V. Zayats, Igor I. Smolyaninov, and Alexei A. Maradudin. Nano-optics of surface plasmon polaritons. *Physics Reports*, 408(3-4):131–314, 2005. doi: 10.1016/j.physrep.2004.11.001.

[28] Jacob B Khurgin. How to deal with the loss in plasmonics and metamaterials. *Nature Nanotechnology*, 10:2–6, 2015. doi: 10.1038/nnano.2014.310.

[29] Ekaterina Y. Lukianova-Hleb, Xiaoyang Ren, Rupa R. Sawant, Xiangwei Wu, Vladimir P. Torchilin, and Dmitri O. Lapotko. On-demand intracellular amplification of chemoradiation with cancer-specific plasmonic nanobubbles. *Nature Medicine*, 20(7):778–784, 2014.

[30] Oara Neumann, Albert D. Neumann, Edgar Silva, Ciceron Ayala-Orozco, Shu Tian, Peter Nordlander, and Naomi J. Halas. Nanoparticle-mediated, light-induced phase separations. *Nano Letters*, 15(12):7880–7885, 2015.

[31] C.-K Sun, F Vallee, L H Acioli, E P Ippen, and J G Fujimoto. Femtosecond-tunable measurement of electron thermalization in gold. *Physical Review B*, 50(15337-15348), 1994.

[32] Min Hu and Gregory V. Hartland. Heat dissipation for au particles in aqueous solution: Relaxation time versus size. *Journal of Physical Chemistry B*, 106 (28):7029–7033, 2002.

[33] Peter Zijlstra, Anna L. Tchebotareva, James W.M. Chon, Min Gu, and Michel Orrit. Acoustic Oscillations and Elastic Moduli of Single Gold Nanorods. *Nano Letters*, 8(10):3493–3497, 2008.

[34] Man-Nung Su, Pratiksha D Dongare, Debadi Chakraborty, Yue Zhang, Chongyue Yi, Fangfang Wen, Wei-Shun Chang, Peter Nordlander, John E Sader, Naomi J Halas, and Stephan Link. Optomechanics of Single Aluminum Nanodisks. *Nano Letters*, 17:2575–2583, 2017.

[35] Mingjie Li, Saikat Bhaumik, Teck Wee Goh, Muduli Subas Kumar, Natalia Yantara, Michael Grätzel, Subodh Mhaisalkar, Nripan Mathews, and Tze Chien Sum. Slow cooling and highly efficient extraction of hot carriers in colloidal perovskite nanocrystals. *Nature Communications*, 8(May):3–12, 2017.

[36] Gaussian beam optics. `https://www.newport.com/n/gaussian-beam-optics`. Accessed: 2021-03-07.

[37] Mark L. Brongersma, Naomi J. Halas, and Peter Nordlander. Plasmon-induced hot carrier science and technology. *Nature Nanotechnology*, 10(1): 25–34, 2015.

[38] A J Nozik. Quantum dot solar cells. *Physica E*, 14:115–120, 2002.

[39] Syed Mubeen, Joun Lee, Nirala Singh, Stephan Krämer, Galen D Stucky, and Martin Moskovits. An autonomous photosynthetic device in which all charge carriers derive from surface plasmons. *Nature Nanotechnology*, 8:247–251, 2013.

[40] Philipp Reineck, Delia Brick, Paul Mulvaney, and Udo Bach. Plasmonic Hot Electron Solar Cells: The Effect of Nanoparticle Size on Quantum Efficiency. *J. Phys. Chem. Lett.*, 7:4137–4141, 2016.

[41] Andrew J Leenheer, Prineha Narang, Nathan S Lewis, and Harry A Atwater. Solar energy conversion via hot electron internal photoemission in metallic nanostructures: Efficiency estimates. *J. Appl. Phys*, 115:1–7, 2014.

[42] Silvia Peruch, Andres Neira, Gregory A. Wurtz, Brian Wells, Viktor A. Podolskiy, and Anatoly V. Zayats. Geometry Defines Ultrafast Hot-Carrier Dynamics and Kerr Nonlinearity in Plasmonic Metamaterial Waveguides and Cavities. *Advanced Optical Materials*, 5(15):1–12, 2017.

[43] Mohammad M. Jadidi, Jacob C. Konig-Otto, Stephan Winnerl, Andrei B. Sushkov, H. Dennis Drew, Thomas E. Murphy, and Martin Mittendorff. Nonlinear Terahertz Absorption of Graphene Plasmons. *Nano Letters*, 16(4):2734–2738, 2016.

[44] M Mehdi Jadidi, Kevin M Daniels, Rachael L Myers-Ward, D Kurt Gaskill, Jacob C Ko Nig-Otto, Stephan Winnerl, Andrei B Sushkov, H Dennis Drew, Thomas E Murphy, and Martin Mittendorff. Optical Control of Plasmonic Hot Carriers in Graphene. *ACS Photonics*, 6:302–307, 2019.

[45] Lisa J Krayer, Elizabeth M Tennyson, Marina S Leite, and Jeremy N Munday. Near-IR Imaging Based on Hot Carrier Generation in Nanometer-Scale Optical Coatings. *ACS Photonics*, 5:306–311, 2018.

[46] Hamidreza Chalabi, David Schoen, and Mark L. Brongersma. Hot-electron photodetection with a plasmonic nanostripe antenna. *Nano Letters*, 14(3): 1374–1380, 2014.

[47] Ali Sobhani, Mark W Knight, Yumin Wang, Bob Zheng, Nicholas S King, Lisa V Brown, Zheyu Fang, Peter Nordlander, and Naomi J Halas. Narrowband photodetection in the near-infrared with a plasmon-induced hot electron device. *Nature Communications*, 4:1–6, 2013.

[48] Peter Nordlander Mark W. Knight, Heidar Sobhani and Naomi J. Halas. Photodetection with Active Optical Antennas. *Science*, 332:702–704, 2011.

[49] Guillaume Baffou and Romain Quidant. Thermo-plasmonics: Using metallic nanostructures as nano-sources of heat. *Laser and Photonics Reviews*, 7(2): 171–187, 2013.

[50] Pierfrancesco Zilio, Michele Dipalo, Francesco Tantussi, Gabriele C Messina, and Francesco De Angelis. Hot electrons in water: injection and ponderomotive acceleration by means of plasmonic nanoelectrodes. *Light: Science & Applications*, 6:1–8, 2017.

[51] Minho Kim, Mouhong Lin, Jiwoong Son, Hongxing Xu, and Jwa Min Nam. Hot-Electron-Mediated Photochemical Reactions: Principles, Recent Advances, and Challenges. *Advanced Optical Materials*, 5(15):1–21, 2017.

[52] Emiliano Cortés, Wei Xie, Javier Cambiasso, Adam S Jermyn, Ravishankar Sundararaman, Prineha Narang, Sebastian Schlücker, and Stefan A Maier. Plasmonic hot electron transport drives nano-localized chemistry. *Nature Communications*, 8:1–10, 2017.

[53] Maria Solera Gerardo A. Lopez, M.-Carmen Estevez and Laura M. Lechuga. Recent advances in nanoplasmonic biosensors: applications and lab-on-a-chip integration. *Nano photonics*, 6(1):123–136, 2016.

[54] Jeffrey N. Anker, W. Paige Hall, Olga lyandres, Nilam C. Shah, Jing Zhao, and Richard P. Van Duyne. Biosensing with plasmonic nanosensors Recent. *Nature Materials*, 7:442–453, 2008.

[55] Phillip Christopher and Martin Moskovits. Hot Charge Carrier Transmission from Plasmonic Nanostructures. *Annu. Rev. Phys. Chem.*, 68:379–398, 2017.

[56] Giulia Tagliabue, Adam S. Jermyn, Ravishankar Sundararaman, Alex J. Welch, Joseph S. DuChene, Ragip Pala, Artur R. Davoyan, Prineha Narang, and Harry A. Atwater. Quantifying the role of surface plasmon excitation and

hot carrier transport in plasmonic devices. *Nature Communications*, 9(1):1–8, 12 2018.

[57] Prineha Narang, Ravishankar Sundararaman, and Harry A. Atwater. Plasmonic hot carrier dynamics in solid-state and chemical systems for energy conversion. *Nanophotonics.*, 5(1):96–111, 2016.

[58] A. Devižis, V. Vaičikauskas, and V. Gulbinas. Ultrafast pump-probe surface plasmon resonance spectroscopy of thin gold films. *Applied Optics*, 45(11): 2535–2539, 2006.

[59] A. Devižis and V. Gulbinas. Ultrafast dynamics of the real and imaginary permittivity parts of a photoexcited silver layer revealed by surface plasmon resonance. *Applied Optics*, 47(10):1632–1637, 2008.

[60] Rogier H. M. Groeneveld, Rudolf Sprik, and Ad Lagendijk. Ultrafast Relaxation of Electrons Probed by Surface Plasmons at a Thin Silver Film. *Physical Review Letters*, 64(7):784–787, 1990.

[61] Gregory V. Hartland. Optical Studies of Dynamics in Noble Metal Nanostructures. *Chemical Reviews*, 111(6):3858–3887, 2011.

[62] Fuming Wang and Nicholas A Melosh. Plasmonic Energy Collection through Hot Carrier Extraction. *Nano Letters*, 11:5426–5430, 2011.

[63] Mohammad Taghinejad, Hossein Taghinejad, Zihao Xu, Yawei Liu, Sean P. Rodrigues, Kyu Tae Lee, Tianquan Lian, Ali Adibi, and Wenshan Cai. Hot-Electron-Assisted Femtosecond All-Optical Modulation in Plasmonics. *Advanced Materials*, 30(9):1–7, 2018.

[64] Jongbum Kim, Enrico G Carnemolla, Clayton Devault, Amr M Shaltout, Daniele Faccio, Vladimir M Shalaev, Alexander V Kildishev, Marcello Ferrera, and Alexandra Boltasseva. Dynamic Control of Nanocavities with Tunable Metal Oxides. *Nano Letters*, 18:740–746, 2018.

[65] Man-Nung Su, Christopher J Ciccarino, Sushant Kumar, Pratiksha D Dongare, Seyyed Ali Hosseini Jebeli, David Renard, Yue Zhang, Behnaz Ostovar, Wei-Shun Chang, Peter Nordlander, Naomi J Halas, Ravishankar Sundararaman, Prineha Narang, and Stephan Link. Ultrafast Electron Dynamics in Single Aluminum Nanostructures. *Nano Letters*, 19:3091–3097, 2019.

[66] Man-Nung Su, Pratiksha D Dongare, Debadi Chakraborty, Yue Zhang, Chongyue Yi, Fangfang Wen, Wei-Shun Chang, Peter Nordlander, John E Sader, Naomi J Halas, and Stephan Link. Optomechanics of Single Aluminum Nanodisks. *Nano Letters*, 17:2575–2583, 2017.

[67] Feng He, Nathanial Sheehan, Seth R. Bank, and Yaguo Wang. Giant electron–phonon coupling detected under surface plasmon resonance in Au film. *Optics Letters*, 44(18):4590–4593, 2019.

[68] Rogier H M Groeneveld, Rudolf Sprik, and Ad Lagendijk. Femtosecond spectroscopy of electron-electron and electron-phonon energy relaxation in Ag and Au. *Physical Review B*, 51:11433–11445, 1995.

[69] Stephan Link and Mostafa A. El-Sayed. Spectral Properties and Relaxation Dynamics of Surface Plasmon Electronic Oscillations in Gold and Silver Nanodots and Nanorods. *Journal of Physical Chemistry B*, 103(40):8410–8426, 1999.

[70] Sungnam Park, Matthew Pelton, Mingzhao Liu, Philippe Guyot-Sionnest, and Norbert F. Scherer. Ultrafast resonant dynamics of surface plasmons in gold nanorods. *Journal of Physical Chemistry C*, 111(1):116–123, 2007.

[71] Michele Ortolani, Andrea Mancini, Arne Budweg, Denis Garoli, Daniele Brida, and Francesco De Angelis. Pump-probe spectroscopy study of ultrafast temperature dynamics in nanoporous gold. *Physical Review B*, 99:1–6, 2019.

[72] S I Anisimov, B L Kapeliovich, T L Perel'man, and L D Landau. Electron emission from metal surfaces exposed to ultrashort laser pulses. *Journal of Experimental and Theoretical Physics*, 39(2):375–377, 1974.

[73] J. Hohlfeld, S.-S. Wellershoff, J. Güdde, U. Conrad, V. Jähnke, and E. Matthias. Electron and lattice dynamics following optical excitation of metals. *Chemical Physics*, 251(1-3):237–258, 2000.

[74] C.-K Sun, F Vallee, L Acioli, E P Ippen, and J G Fujimoto. Femtosecond investigation of electron thermalization in gold. *Physical Review B*, 48:12365–12368, 1993.

[75] Neil W Ashcroft and N David. Mermin. *Solid state physics*. New York : Holt, Rinehart and Winston, 1976.

[76] Harsha Reddy, Urcan Guler, Alexander V Kildishev, Alexandra Boltasseva, Vladimir M Shalaev, J A Schuller, E S Barnard, W Cai, Y C Jun, J S White, and M L Brongersma. Temperature-dependent optical properties of gold thin films. *Optics Express*, 6(9):2776–2802, 2016.

[77] The frequency and temperature dependence of the optical effective mass of conduction electrons in simple metals. *Journal of Physics and Chemistry of Solids*, 30(12):2765–2769, 1969.

[78] Peijun Guo, Richard D Schaller, John B Ketterson, and Robert P H Chang. Ultrafast switching of tunable infrared plasmons in indium tin oxide nanorod arrays with large absolute amplitude. *Nature Photonics*, 10:267–274, 2016.

[79] J A Woollam Co. CompleteEASE™ Data Analysis Manual. Technical report, 2004. URL `http://www.jawoollam.com`.

[80] Lan Jiang and Hai-Lung Tsai. Improved Two-Temperature Model and Its Application in Ultrashort Laser Heating of Metal Films. *Journal of Heat Transfer*, 127:1167–1173, 2005.

[81] J. K. Chen and J. E. Beraun. Numerical study of ultrashort laser pulse interactions with metal films. *Numer. Heat TR. A-Appl.*, 40(1):1–20, 2001.

[82] Zhibin Lin, Leonid V Zhigilei, and Vittorio Celli. Electron-phonon coupling and electron heat capacity of metals under conditions of strong electron-phonon nonequilibrium. *Physical Review B*, 77(075133):1–17, 2008.

[83] Nicki Hogan, Shengxiang Wu, and Matthew Sheldon. Photothermalization and hot electron dynamics in the steady state. *Journal of Physical Chemistry C*, 124:4931–4945, 2020.

[84] Ana M Brown, Ravishankar Sundararaman, Prineha Narang, William A Goddard Iii, and Harry A Atwater. Ab initio phonon coupling and optical response of hot electrons in plasmonic metals. *Physical Review B*, 94:75120, 2016.

[85] Ye Yang, David P Ostrowski, Ryan M France, Kai Zhu, Jao Van De Lagemaat, Joseph M Luther, and Matthew C Beard. Observation of a hot-phonon bottleneck in lead-iodide perovskites. *Nature Photonics*, 10:53–59, 2016.

[86] S. J. Oldenburg, R. D. Averitt, S. L. Westcott, and N. J. Halas. Nanoengineering of optical resonances. *Chemical Physics Letters*, 288:243–247, 1998.

[87] S. A. Maier, M. L. Brongersma, P. G. Kik, S. Meltzer, A. A.G. Requicha, and H. A. Atwater. Plasmonics - A route to nanoscale optical devices. *Advanced Materials*, 13(19):1501–1505, 2001.

[88] Vivian E. Ferry, Jeremy N. Munday, and Harry A. Atwater. Design considerations for plasmonic photovoltaics. *Advanced Materials*, 22(43):4794–4808, 2010.

[89] Xiang Zhang Nicholas Fang, Hyesog Lee, Cheng Sun. Sub–Diffraction-Limited Optical Imaging with a Silver Superlens. *Science*, 308:534–538, 2005.

[90] Vladimir M. Shalaev, W. Cai, U. Chettiar, H. K. Yuan, A. K. Sarychev, V. P. Drachev, and A. V. Kildishev. Negative index of refraction in optical metamaterials. *Optics letters*, 30(24):3356–3358, 2005.

[91] David O. S. Melville and Richard J. Blaikie. Super-resolution imaging through a planar silver layer. *Optics Express*, 13(6):2127, 2005.

[92] Yaocai Bai, Chuanbo Gao, and Yadong Yin. Fully alloyed Ag/Au nanorods with tunable surface plasmon resonance and high chemical stability. *The Royal Society of Chemistry*, 9:14875 – 14880, 2017.

[93] Xiaotian Wang, Guanshui Ma, Anran Li, Jian Yu, Zhao Yang, Jie Lin, Ang Li, Xiaodong Han, and Lin Guo. Composition-adjustable Ag-Au substitutional alloy microcages enabling tunable plasmon resonance for ultrasensitive SERS. *Chemical Science*, 9:4009 – 4015, 2018.

[94] Chen Gong and Marina S. Leite. Noble Metal Alloys for Plasmonics. *ACS Photonics*, 3(4):507–513, 2016.

[95] Chen Gong, Alan Kaplan, Zackery A. Benson, David R. Baker, Joshua P. McClure, Alexandre R. Rocha, and Marina S. Leite. Band Structure Engineering by Alloying for Photonics. *Advanced Optical Materials*, 6(17):1–7, 2018.

[96] Mukesh Kumar, Satoshi Ishii, Naoto Umezawa, and Tadaaki Nagao. Band engineering of ternary metal nitride system $Ti_{1-x}Zr_xN$ for plasmonic applications. *Optical Materials Express*, 6(1):29, 2016.

[97] Cun Zheng Ning Peidong Yang, Letian Dou, and Peidong Yang. Bandgap engineering in semiconductor alloy nanomaterials with widely tunable compositions. *Nature Reviews Materials*, 2:1–15, 2017.

[98] Tao Gong and Jeremy N Munday. Angle-Independent Hot Carrier Generation and Collection Using Transparent Conducting Oxides. *Nano Letters*, 15:147–152, 2015.

[99] Mariama Rebello Sousa Dias, Chen Gong, Zackery A. Benson, and Marina S. Leite. Lithography-Free, Omnidirectional, CMOS-Compatible AlCu Alloys for Thin-Film Superabsorbers. *Advanced Optical Materials*, 6(2):1700830, jan 2018.

[100] Jun Ando, Akihiko Nakamura, Mayuko Yamamoto, Chihong Song, Kazuyoshi Murata, and Ryota Iino. Multicolor High-Speed Tracking of Single Biomolecules with Silver, Gold, and Silver-Gold Alloy Nanoparticles. *ACS Photonics*, 6:2870–2883, 2019.

[101] Mitsuo Niinomi, Masaaki Nakai, and Junko Hieda. Development of new metallic alloys for biomedical applications. *Acta Biomaterialia*, 8(11):3888–3903, 2012.

[102] Xiangwen Liu, Dingsheng Wang, and Yadong Li. Synthesis and catalytic properties of bimetallic nanomaterials with various architectures. *Nano Today*, 7:448–466, 2012.

[103] Dingsheng Wang and Yadong Li. Bimetallic Nanocrystals: Liquid-Phase Synthesis and Catalytic Applications. *Advanced Materials*, 23(9):1044–1060, mar 2011.

[104] P. Hernández-Fernández, S. Rojas, P. Ocón, J. L.Gómez De La Fuente, J. San Fabián, J. Sanza, M. A. Peña, F. J. García-García, P. Terreros, and J. L.G.

Fierro. Influence of the preparation route of bimetallic Pt-Au nanoparticle electrocatalysts for the oxygen reduction reaction. *Journal of Physical Chemistry C*, 111(7):2913–2923, 2007.

[105] Cheng Zhang, Dewei Zhao, Deen Gu, Hyunsoo Kim, Tao Ling, Yi Kuei Ryan Wu, and L. Jay Guo. An ultrathin, smooth, and low-loss Al-doped Ag film and its application as a transparent electrode in organic photovoltaics. *Advanced Materials*, 26(32):5696–5701, 2014.

[106] Carl Wadell, Ferry Anggoro Ardy Nugroho, Emil Lidstro, Beniamino Iandolo, Jakob B Wagner, and Christoph Langhammer. Hysteresis-Free Nanoplasmonic Pd-Au Alloy Hydrogen Sensors. *Nano Letters*, 15:3570, 2015.

[107] Ferry A.A. Nugroho, Iwan Darmadi, Lucy Cusinato, Arturo Susarrey-Arce, Herman Schreuders, Lars J. Bannenberg, Alice Bastos da Silva Fanta, Shima Kadkhodazadeh, Jakob B. Wagner, Tomasz J. Antosiewicz, Anders Hellman, Vladimir P. Zhdanov, Bernard Dam, and Christoph Langhammer. Metal–polymer hybrid nanomaterials for plasmonic ultrafast hydrogen detection. *Nature Materials*, 18(5):489–495, may 2019.

[108] Kevin J Palm, Joseph B Murray, Joshua P Mcclure, Marina S Leite, and Jeremy N Munday. In Situ Optical and Stress Characterization of Alloyed Pd_xAu_{1-x} Hydrides. *ACS Appl. Mater. Interfaces*, 11:45057–45067, 2019.

[109] Yoshiaki Nishijima, Shogo Shimizu, Keisuke Kurihara, Yoshikazu Hashimoto, Hajime Takahashi, Armandas Balcytis, Gediminas Seniutinas, Shinji Okazaki, Jurga Juodkazyt, Takeshi Iwasa, Tetsuya Taketsugu, Yoriko Tominaga, Saulius Juodkazis, S K Earl, T D James, T J Davis, J C McCallum, R E Marvel, R F Haglund, and A Roberts. Optical readout of hydrogen storage in films of Au and Pd. *Optics Express*, 7(25):24081, 2015.

[110] Ravishankar Sundararaman, Prineha Narang, Adam S Jermyn, William A Goddard III, and Harry A Atwater. Theoretical predictions for hot-carrier generation from surface plasmon decay. *Nature Communications*, 5:1–8, 2014.

[111] Jose H Hodak, Arnim Henglein, and Gregory V Hartland. Photophysics of Nanometer Sized Metal Particles: Electron-Phonon Coupling and Coherent Excitation of Breathing Vibrational Modes. *Journal of Physical Chemistry B*, 104:9954–9965, 2000.

[112] Christophe Voisin, Natalia Del Fatti, Dimitris Christofilos, and Fabrice Vallée. Ultrafast Electron Dynamics and Optical Nonlinearities in Metal Nanoparticles. *Journal of Physical Chemistry B*, 105:2264–2280, 2001.

[113] Alberto Naldoni, Francesca Riboni, Urcan Guler, Alexandra Boltasseva, Vladimir M Shalaev, and Alexander V Kildishev. Solar-Powered Plasmon-Enhanced Heterogeneous Catalysis. *Nanophotonics*, 5:112–133, 2016.

[114] Prashant K. Jain, Ivan H. ElSayed, and Mostafa A. El-Sayed. Au nanoparticles target cancer. *Nano Today*, 2(1):18–29, 2007.

[115] Gang Han, Partha Ghosh, and Mrinmoy M De Vincent Rotello. Drug and Gene Delivery using Gold Nanoparticles. *Nanobiotechnol*, 3:40–45, 2007.

[116] Otto L Muskens, Luca Bergamini, Yudong Wang, Jeffrey M Gaskell, Nerea Zabala, C H De Groot, David W Sheel, and Javier Aizpurua. Antenna-assisted picosecond control of nanoscale phase transition in vanadium dioxide. *Light: Science and Applications*, 5:1–9, 2016.

[117] Fuming Wang and Nicholas A Melosh. Plasmonic Energy Collection through Hot Carrier Extraction. *Nano Letters*, 11:5426–5430, 2011.

[118] Wei Li and Jason Valentine. Metamaterial Perfect Absorber Based Hot Electron Photodetection. *Nano Letters*, 14:3510–3514, 2014.

[119] Anshu Pandey and Philippe Guyot-Sionnest. Slow Electron Cooling in Colloidal. *Science*, 322(November):929–932, 2008.

[120] G. J. Conibeer, D. König, M. A. Green, and J. F. Guillemoles. Slowing of carrier cooling in hot carrier solar cells. *Thin Solid Films*, 516:6948, 2008.

[121] Zachary J Coppens, Wei Li, D Greg Walker, and Jason G Valentine. Probing and Controlling Photothermal Heat Generation in Plasmonic Nanostructures. *Nano Letters*, 13:1023–1028, 2013.

[122] David Rioux, Simon Vallières, Sébastien Besner, Philip Muñoz, Eric Mazur, and Michel Meunier. An analytic model for the dielectric function of Au, Ag, and their Alloys. *Advanced Optical Materials*, 2(2):176–182, 2014.

[123] Sarvenaz Memarzadeh, Jongbum Kim, Yigit Aytac, Thomas Murphy, and Jeremy Munday. Surface Plasmon Assisted Control of Hot-Electron Relaxation Time. *Optica*, 7(6), 2020.

[124] Paul R. West, Satoshi Ishii, Gururaj V. Naik, Naresh K. Emani, Vladimir M. Shalaev, and Alexandra Boltasseva. Searching for better plasmonic materials. *Laser and Photonics Reviews*, 4(6):795–808, 2010.

[125] Kevin M Mcpeak, Sriharsha V Jayanti, Stephan J P Kress, Stefan Meyer, Stelio Iotti, Aurelio Rossinelli, and David J Norris. Plasmonic Films Can Easily Be Better: Rules and Recipes. *ACS Photonics*, 2:326–333, 2015.

[126] Yoshiaki Nishijima and Shunsuke Akiyama. Unusual optical properties of the Au/Ag alloy at the matching mole fraction. *Optical Materials Express*, 2(9): 1226–1235, 2012.

[127] Dmitry I. Yakubovsky, Aleksey V. Arsenin, Yury V. Stebunov, Dmitry Yu. Fedyanin, and Valentyn S. Volkov. Optical constants and structural properties of thin gold films. *Optics Express*, 25(21):25574, 2017.

[128] Olivier Pluchery, Romain Vayron, and Kha-Man Van. Laboratory experiments for exploring the surface plasmon resonance. *Eur. J. Phys.*, 32:585, 2011.

[129] C. K. Sun, F. Vallée, L. H. Acioli, E. P. Ippen, and J. G. Fujimoto. Femtosecond-tunable measurement of electron thermalization in gold. *Physical Review B*, 50(20):15337–15348, 1994.

[130] Evangelina Pensa, Julian Gargiulo, Alberto Lauri, Sebastian Schlücker, Emiliano Cortés, and Stefan A. Maier. Spectral Screening of the Energy of Hot Holes over a Particle Plasmon Resonance. *Nano Letters*, 19(3):1867–1874, 2019.

[131] Tao Gong and Jeremy N Munday. Materials for hot carrier plasmonics. *Optical Materials Express*, 5(11):2501–2512, 2015.

[132] Lisa J. Krayer, Kevin J. Palm, Chen Gong, Alberto Torres, Cesar E.P. Villegas, Alexandre R. Rocha, Marina S. Leite, and Jeremy N. Munday. Enhanced near-Infrared Photoresponse from Nanoscale Ag-Au Alloyed Films. *ACS Photonics*, 7(7):1689–1698, 2020.

[133] Peijun Guo, Richard D Schaller, John B Ketterson, and Robert P H Chang. Ultrafast switching of tunable infrared plasmons in indium tin oxide nanorod arrays with large absolute amplitude. *Nature Photonics*, 10(4):267–274, 2016.

[134] Deen Gu, Cheng Zhang, Yi Kuei Wu, and L. Jay Guo. Ultrasmooth and thermally stable silver-based thin films with subnanometer roughness by aluminum doping. *ACS Nano*, 8(10):10343–10351, 2014.

[135] Jose Hodak, Ignacio Martini, and Gregory V Hartland. Ultrafast study of electron-phonon coupling in colloidal gold particles. *Chemical Physics Letters*, 284:135–141, 1998.

[136] Marcos M Alvarez, Joseph T Khoury, T Gregory Schaaff, Marat N Shafigullin, Igor Vezmar, and Robert L Whetten. Optical Absorption Spectra of Nanocrystal Gold Molecules. *Journal of Physical Chemistry B*, 101:3706–3712, 1997.

[137] H. J. Eichler, D. Langhans, and F. Massmann. Coherence peaks in picosecond sampling experiments. *Optics Communications*, 50(2):117–122, 1984.

[138] Gururaj V. Naik, Vladimir M. Shalaev, and Alexandra Boltasseva. Alternative plasmonic materials: Beyond gold and silver. *Advanced Materials*, 25(24): 3264–3294, 2013.

[139] Alexandra Boltasseva, Atwater, and Harry A. Low-Loss Plasmonic Metamaterials. *Science*, 331(January):290–292, 2011.

[140] Orad Reshef, Israel De Leon, M. Zahirul Alam, and Robert W. Boyd. Nonlinear optical effects in epsilon-near-zero media. *Nature Reviews Materials*, 4 (8):535–551, 2019.

[141] Salvatore Campione, Igal Brener, and Francois Marquier. Theory of epsilon-near-zero modes in ultrathin films. *Physical Review B - Condensed Matter and Materials Physics*, 91(12):1–5, 2015.

[142] Benjamin T. Diroll, Soham Saha, Vladimir M. Shalaev, Alexandra Boltasseva, and Richard D. Schaller. Broadband Ultrafast Dynamics of Refractory Metals: TiN and ZrN. *Advanced Optical Materials*, 8(19):1–9, 2020.